SIMULATIONS AND MEASUREMENTS OF X-BAND ACCELERATING STRUCTURES FOR THE CLIC PROJECT

A Thesis Submitted to
the Graduate School of Engineering and Sciences of
İzmir Institute of Technology
in Partial Fulfillment of the Requirements for the Degree of

MASTER OF SCIENCE

in Electronics and Communication Engineering

by
Hikmet BURSALI

July 2018
İZMİR

We approve the thesis of **Hikmet BURSALI**

Examining Committee Members:

Asst. Prof. Dr. Fatih YAMAN
Department of Electrical-Electronics Engineering, Izmir Institute of Technology

Dr. Nuria CATALAN LASHERAS
BE-RF-MK, European Organisation for Nuclear Research (CERN)

Prof. Dr. Alp KUŞTEPELİ
Department of Electrical-Electronics Engineering, İzmir Institute of Technology

Prof. Dr. M. Salih DİNLEYİCİ
Department of Electrical-Electronics Engineering, İzmir Institute of Technology

Asst. Prof. Dr. Avni AKSOY
Institute of Accelerator Technologies, Ankara University

9 July 2018

Asst. Prof. Dr. Fatih YAMAN
Supervisor, Department of Electrical
-Electronics Engineering
İzmir Institute of Technology

Dr. Nuria CATALAN LASHERAS
Cosupervisor, BE-RF-MK
CERN

Prof. Dr. Enver TATLICIOĞLU
Head of the Department of
Electrical and Electronics Engineering

Prof. Dr. Aysun SOFUOĞLU
Dean of the Graduate School of
Engineering and Sciences

ACKNOWLEDGMENTS

I would like to thank to my working group at CERN and especially my supervisor Dr. Nuria Catalan Lasheras for her patience and help during my work.

I would like to thank also Dr. Walter Wuensch, Dr. Alexej Grudiev, Dr. Rolf Wegner, Dr. Joel Sauza Bedolla for their valuable advices.

Also, I would like to thank to my supervisor Asst. Prof. Dr. Fatih YAMAN for his help and confidence during my Master's study.

Finally, I am grateful to my family for their support and confidence.

ABSTRACT

SIMULATIONS AND MEASUREMENTS OF X-BAND ACCELERATING STRUCTURES FOR THE CLIC PROJECT

The Compact Linear Collider (CLIC) Project is 50 km long e^-, e^+ linear collider planned to be built in three stages with 3 TeV center-of-mass energy at its last stage. The CLIC accelerator includes around 140000 accelerating structures. The cost optimisation process is ongoing before the production stage.

In order to obtain the CLIC design requirements, the accelerating structures are machined out of OFE copper and ultra precision turning and milling with single diamond tool. The required precision on the order of the micron makes the final product relatively expensive. The assembly of these copper parts is done by electron beam welding of two halves or diffusion bonding of disc stacks.

In this thesis we investigate the potential geometrical correlation between the imperfection of the accelerating structure discs inner radii and their individual frequency deviations before and after bonding.

Following the results of this work, the tolerance study of the machining and bonding effects will be understood and manufacturing process will be optimised for cost saving.

ÖZET

CLIC PROJESİ X-BANT HIZLANDIRICI YAPILARI İÇİN SİMÜLASYONLAR VE ÖLÇÜMLER

Sıkışık Doğrusal Çarpıştırıcı (CLIC) Projesi son aşamasında 3 TeV çarpışma enerjisine ulaşması planlanan 3 aşamalı 50 km uzunluğunda doğrusal bir e^-, e^+ çarpıştırıcısıdır. CLIC hızlandırıcısı son aşamasında 140000 civarında hızlandırıcı yapısı içermektedir. Üretim aşamasına geçilmeden önce maliyet iyileştirme çalışmaları devam etmektedir.

CLIC Projesi tasarım parametrelerini elde etmek için, hızlandırıcı yapıları oksijen içermeyen (OFE) bakırdan tekli elmas uç kullanılarak ultra hassas makine işleme teknikleri ile üretilmektedir. Gerekli olan mikrometre düzeydeki hassasiyet, bu yapıları son üretim aşamasında çok pahalı hale getirmektedir. Bu hızlandırıcı yapıların bakır parçaların montajı iki yarım şeklinde elektron kaynağı ya da disk olarak üretilip difüzyon bağlama ile yapılmaktadır.

Bu tezde hızlandırıcı disk yapılarının iç yarıçaplarındaki bozulmalar ile aynı disklerin frekans sapmaları arasındaki olası korelasyon difüzyon bağlama işleminin öncesi ve sonrası için araştırıldı.

Bu çalışmanın sonuçları, makine işleme hassasiyeti ve difüzyon bağlama işleminin etkisinin anlaşılıp üretim maliyetinin iyileştirilmesi için kullanılacaktır.

TABLE OF CONTENTS

LIST OF FIGURES

LIST OF TABLES

LIST OF ABBREVIATIONS

CERN	Conseil Européen pour la Recherche Nucléaire
CLIC	Compact Linear Collider
FCC	Future Circular Collider
LHC	Large Hadron Collider
LINAC	Linear Accelerator
RF	Radio Frequency
VNA	Vector Network Analyzer
TeV	Tera Electron Volt
GeV	Giga Electron Volt
BDR	Breakdown Rate
TE-VSC	Technology Department-Vacuum Surface Coating

CHAPTER 1

INTRODUCTION

In this chapter, the accelerating structure manufacturing process and motivation of thesis are presented with a brief mention of CERN and CLIC Study.

1.1. CERN

The European Scientific Laboratory for Nuclear Research as known in French *'Conseil Européen pour la Recherche Nucléaire'* (CERN) is established after an intergovernmental meeting of UNESCO in Paris in December 1951. The location of the CERN was decided at canton of Geneva and the facilities were built at Swiss-French border. It is the scientific organisation that includes the largest particle physics laboratory of the world. CERN has 22 member states, 8 associate member states and 2 observer states as an international organisation. Turkey is an associate member of CERN since 6th of May 2015.

CERN was officially established on 29th of September 1954 by 12 Founder Member States; Belgium, Denmark, France, the Federal Republic of Germany, Greece, Italy, the Netherlands, Norway, Sweden, Switzerland, the United Kingdom, and Yugoslavia. In 1957, the first accelerator of CERN, the Synchrocyclotron started to operate and continued to operate until 1990. Besides it was especially focused on particle physics after 1957. In 1969, the Proton Synchrotron started to operate and was used for the research related to particle physics [1]. The latest accelerator of CERN is Large Hadron Collider (LHC) that has four collision detectors ALICE, ATLAS, CMS, LHCb. It was designed to get an information related to refinement of the standard model. It is still in operation from September 2008 [2]. CERN has about 2.250 staff members; however, this amount is getting close to 13.000 users with PhD students, fellows, technical students and other visitor scientists from different countries. CERN has two main ongoing studies for future that are still in planning and research;

- FCC ; 80-100 km circular collider that will provide hadron collisions up to 100 TeV [3].

- CLIC; 50 km linear electron(e-)-positron(e+)collider that will allow 3 TeV nominal total energy for collisions [4].

1.2. CLIC Study

The Compact Linear Collider (CLIC) is a linear electron-positron collider that is under research and development as an international collaboration that has 43 partners in 22 countries at CERN. CLIC study has established in order to obtain new particles from the collisions of electrons and their antimatter, positrons to complement the Large Hadron Collider (LHC) results. CLIC has been designed with three center of mass energy stages for collisions; 380 GeV, 1.5 TeV and 3 TeV as a programme spanning 22 years. The aim of CLIC study is to develop an accelerating structures that have 100 MV/m loaded gradient capability to reach 3 TeV nominal total energy for obtaining new particles after electron-positron collisions by using two-beam accelerating concept. It aims also improving the material science with breakdown research, ultra precision machining, precise alignment and RF technologies [4].

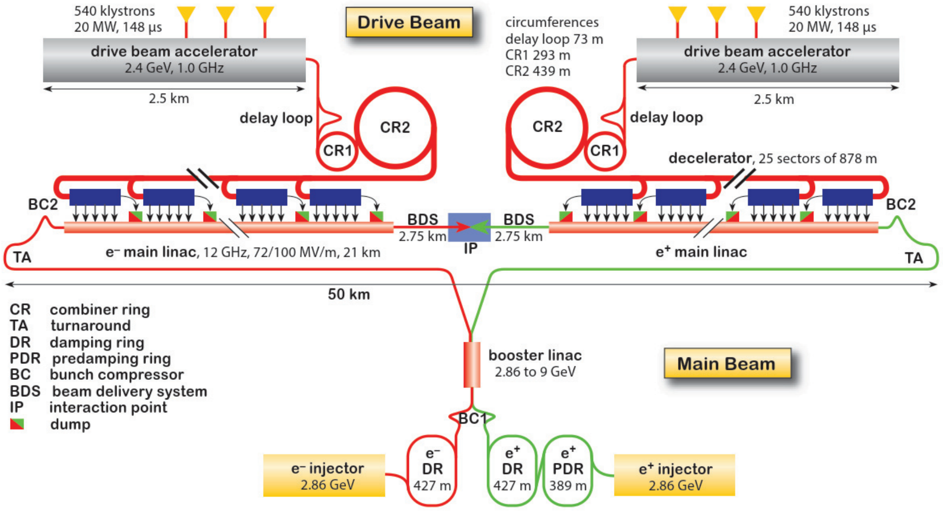

Figure 1.1. CLIC Layout at 3 TeV [5]

The two beam acceleration concept means that the main beam accelerating structures which accelerates the positrons and electrons are fed by another drive beam that its power is transferred by RF systems as illustrated in the Figure 1.2. The Drive Beam uses electron beam for acceleration and RF power is extracted from these electron beam by PETS (Power Extraction and Transfer Structures) that are special RF components.

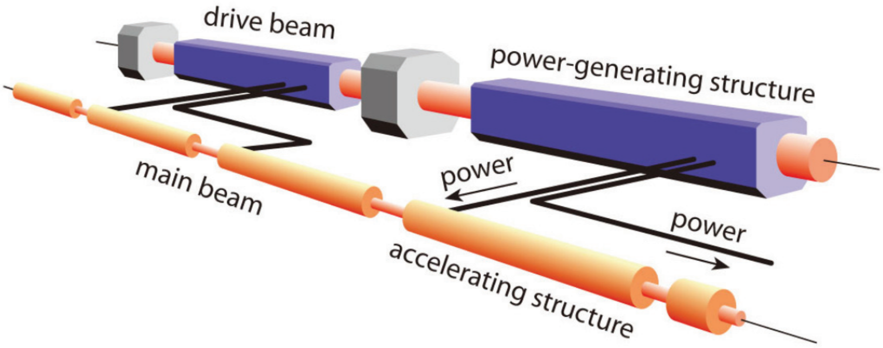

Figure 1.2. CLIC two beam scheme [5]

The CLIC study has three main energy stages for collisions as mentioned before; 380 GeV, 1.5 TeV and 3 TeV. The total length of these three stages are 11.4, 29.0 and 50.1 km respectively.

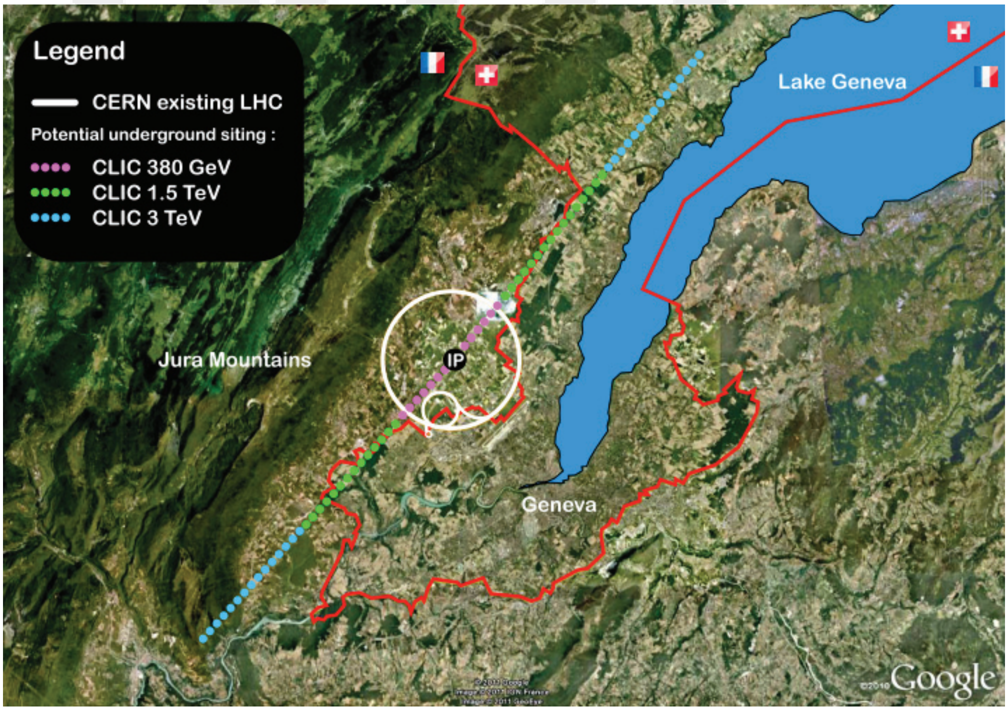

Figure 1.3. Location of CLIC Stages on Map

CLIC Study totally includes 142812 accelerating structures for the third stage and one of the main challenges of it is cost optimisation.

1.3. Radio-Frequency Accelerating Structures

The Radio-Frequency (RF) accelerating structures are one of the main working topics about all the particle colliders. They are metal structures that have been using for accelerating the several kind of subatomic particles by RF power. Accelerating structures can be divided in two main groups as circular and linear accelerators. In this thesis linear accelerators were studied and presented. The first study about accelerators was conducted by G. Ising, he proposed a system that had sequentially pulsed drift tubes where the particle beams could be accelerated in gaps between the tubes in 1924. Then the first prototype of linacs was presented by Wideröe in 1927 at Aachen, Germany. The working principle of it was based on time-varying electric fields and it was composed of drift tubes as illustrated in Figure 1.4 given below, this work proved the system that Ising proposed in 1924 [6].

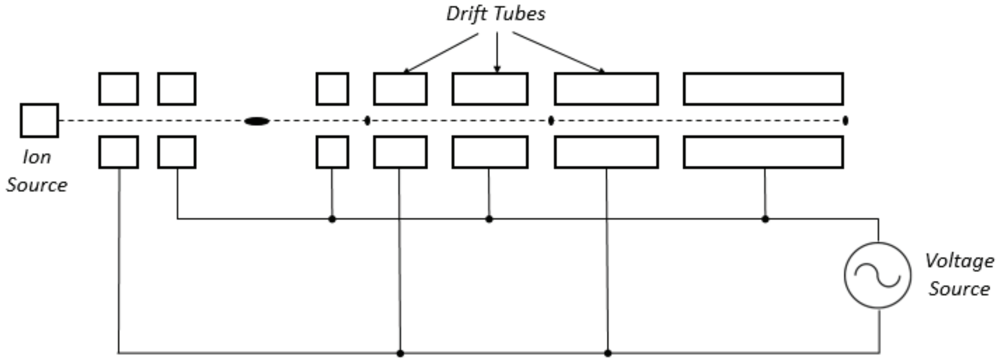

Figure 1.4. Concept of Wideröe drift tube linac

The RF linacs did not only utilized in scientific areas but also, they were used in medical and industrial areas such as ion production, radiation measurement, medical diagnostics, cancer treatment (radiotherapy), stress analysis of aircrafts.

1.3.1. Electromagnetism and Cavity Modes

The improvement of modern electromagnetism is based on the formulas as given below in differential form represented by J. Clerk Maxwell in 19^{th} century.

$$\nabla.\vec{E} = \frac{1}{\varepsilon}\rho \tag{1.1}$$

$$\nabla.\vec{B} = 0 \tag{1.2}$$

$$\nabla \times \vec{E} = -\frac{\partial \vec{B}}{\partial t} \tag{1.3}$$

$$\nabla \times \vec{B} = \mu(\vec{J} + \varepsilon\frac{\partial \vec{E}}{\partial t}) \tag{1.4}$$

These four fundamental formulas describe the electromagnetism by identifying the interactions of electric and magnetic fields and propagation type as wave. In formulas, E and B represent electric and magnetic fields. J represents current density and ρ represents the distribution of charge. ε and μ represent electric permittivity and magnetic permeability of the physical medium respectively. To obtain electromagnetic fields these formulas can be solved for different kind of geometries using boundary conditions. However analytical solutions of such types of problems can be found only for certain simple domains, for example, sphere, cylinder, rectangle. For more complicated structures numerical methods should be applied to solve the Maxwell equations at a certain level of accuracy.

To produce the accelerating field, the electromagnetic field must be bounded with a highly conducting material to confine in a metal structure that is called cavity resonators. The distribution of electromagnetic field inside the cavity is called mode. Modes can be grouped as:

- TM mode: Transverse magnetic mode is characterized by B=0 in the direction of propagation.
- TE mode: Transverse electric mode is characterized by E=0 in the direction of propagation.
- TEM mode: Transverse electric magnetic mode is characterized by both E=0 and B=0 in the direction of propagation [6].

For accelerating structures, generally TM_{010} mode is used because it has suitable electric and magnetic field distribution to obtain accelerating field as shown in Figure 1.4. The cavity type of linacs are chosen as circular form and they are produced according to required design parameters.

As illustrated in Figure 1.5, pillbox cavities are chosen as accelerator cavities. Generally, the other linacs are combining of pillbox cavities sequentially.

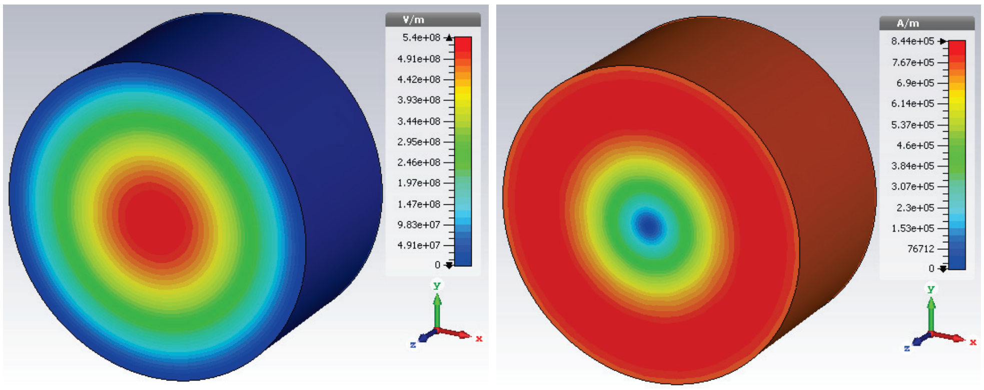

Figure 1.5. Pillbox cavity, Electric (left) and Magnetic Field Distribution of TM$_{010}$ mode obtained via CST MWS [7]

1.3.2. Synchronism of Particle Beam and Accelerating Field

Uniform waveguides are defined by their cut-off frequency above which electromagnetic wave are propagated. Waves with lower frequency are decaying exponentially in the waveguide. Cut-off frequency formula for uniform circular waveguides for TE and TM modes are given by the formulas 1.5, 1.6 respectively where p_{nm} and $p^{'}_{nm}$ represents roots of the Bessel functions;

$$f_{c_{nm}} = \frac{k_c}{2\pi\sqrt{\mu\epsilon}} = \frac{p^{'}_{nm}}{2\pi a\sqrt{\mu\epsilon}} \tag{1.5}$$

$$f_{c_{nm}} = \frac{k_c}{2\pi\sqrt{\mu\epsilon}} = \frac{p_{nm}}{2\pi a\sqrt{\mu\epsilon}} \tag{1.6}$$

The condition of propagation inside a uniform waveguide;

$$\omega > \omega_c \tag{1.7}$$

During the observation of an oblique incident wave in a uniform waveguide as illustrated in Figure 1.6, we see that there is an interference between incident wave and reflected wave from the conducting boundary in the direction of propagation (z direction).

When observing the distance between two adjacent crests created by interference, the wavelength of phase velocity λ_p is greater than the wavelength of incident oblique wave λ as shown in Figure 1.7. The phase velocity of a wave inside the uniform waveguide is greater than the speed of light.

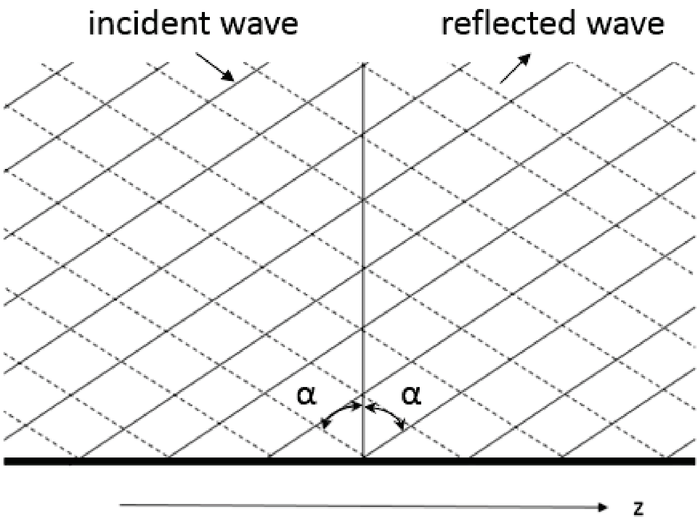

Figure 1.6. Oblique wave incidence in the z propagation direction

$$v_{ph} = \frac{\omega}{k} \tag{1.8}$$

$$v_{ph} = \frac{\lambda_p}{\lambda} c = \frac{c}{\sin \alpha} > c \tag{1.9}$$

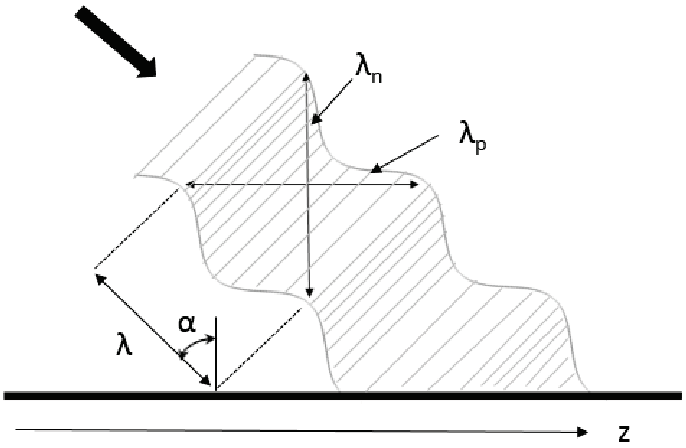

Figure 1.7. Incident wave with a wavelength λ; λ_p and λ_n represents the wavelengths that are parallel and perpendicular to the conducting boundary

The dispersion equation describes the effects of the dispersion in a medium of an electromagnetic wave which is traveling through that medium for a uniform waveguide [9];

$$\omega^2 = \omega_c^2 + (k_0 c)^2 \tag{1.10}$$

where k_0 is the wave number of the wave that is propagating in vacuum.

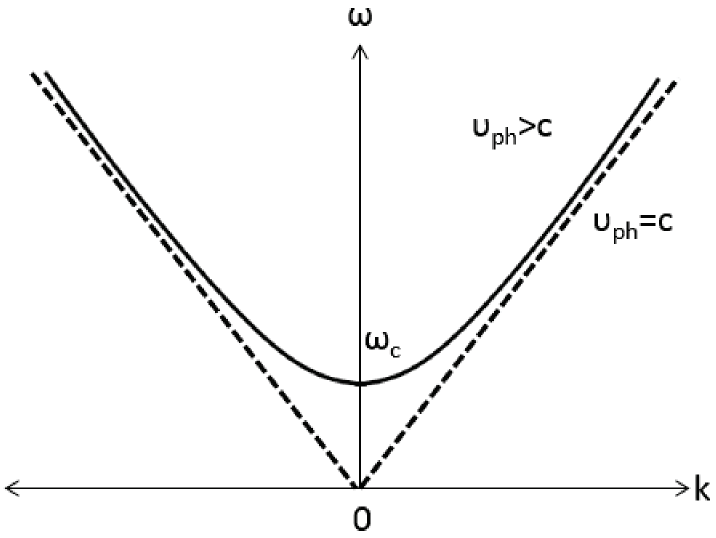

Figure 1.8. Dispersion (Brillouin) Diagram for uniform waveguide

1.3.3. Periodic Accelerating Structures

In order to obtain the acceleration, phase velocity must be synchronised with the speed of the accelerated particles which is closer to the speed of light. After synchronisation of the phase velocity and particles velocity, the maximum electric field can be matched and used for acceleration. The solution is to make obstacles inside the waveguide to slow the phase velocity and to use the maximum accelerating field.

The periodic accelerating structures can be divided in two groups according to their working principle; standing wave and traveling wave structures. In a standing wave working principle, the RF field inside the structure is created in the whole structure simultaneously and there is no propagation of electromagnetic energy. In traveling wave working principle, the RF field and energy are both transferred through the structure. The traveling wave structures need an external load to absorb the transferred RF energy along it. The travelling wave structures are divided in two groups; constant impedance and constant gradient structures. The constant impedance structures are composed of geometrically uniform cells and this causes the decreasing of both power and gradient through the structure. The constant gradient structures are tapered structures from input to output. With the advantage of this tapering shape, RF field can confine better inside the structure compare to constant impedance structures.

The traveling wave accelerating structures are composed of identical cells that are separated by irises for electrical coupling between each other. The RF signal enters from the input cell and propagates along beam direction by confining the inner walls of the structure. The RF field is absorbed by the beam and structure inner walls, so the amplitude of the field is getting smaller through the end of the structure. Then, it goes out from the output cell and suppressed at the resistive loads that are connected to the output of the structure.

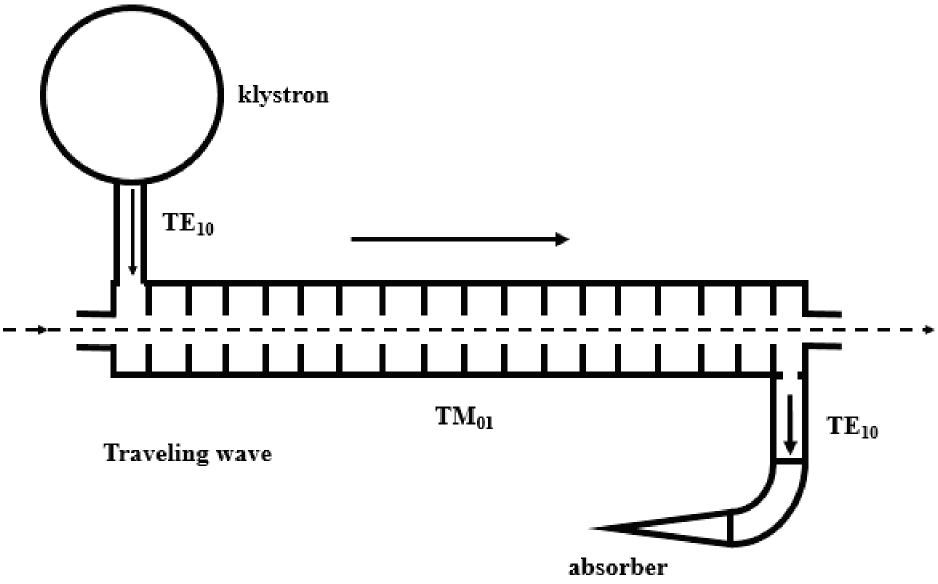

Figure 1.9. Traveling Wave Linac Scheme [8]

The operating modes of the structures are identified by the distance between two peak values of the fields that is called phase advance (see Section 2). According to Floquet's Theorem which states that in a given operating mode of a wave oscillation and at an operating frequency, the wave function can be multiplied by a constant ($e^{\gamma L}$ where $\gamma = \alpha + jk_0$, L is the length of cell, k_0 is the wave number in free space) which is generally complex when the wave passing from one period to the next [6].

After placing the discs inside the uniform structure with spacing L, the dispersion relation for a loaded periodic structure becomes;

$$\omega^2 = \omega_c^2 + (k_0 + \frac{2\pi n}{L})^2 \tag{1.11}$$

The phase velocity in the periodic structure and the dispersion curve becomes;

$$\upsilon_{ph} = \frac{\omega}{k_0 + 2\pi n/L} = \frac{\omega}{k_n} \tag{1.12}$$

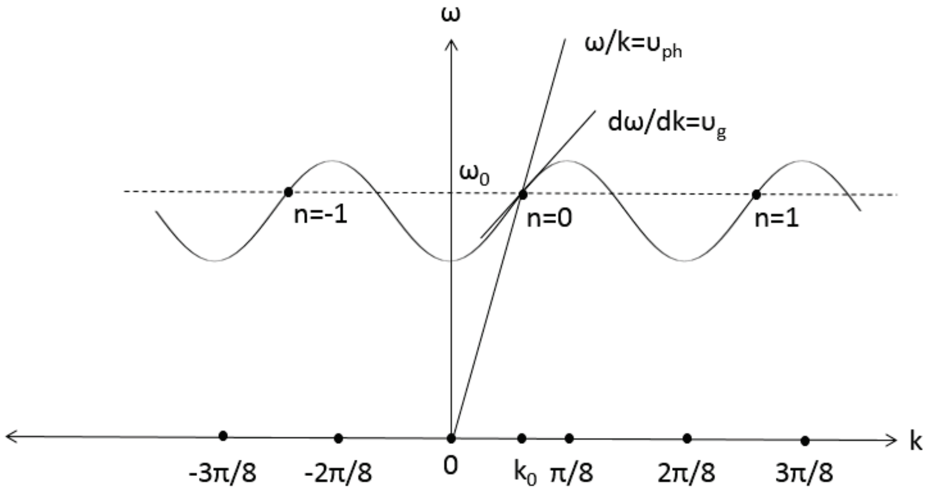

Figure 1.10. Dispersion curve for iris loaded structure

With the suitable spacing L of the discs, the phase velocity can be set as desired. Then, the traveling wave linac can be designed. In this thesis two CLIC main accelerating structures were studied, T24 and TD26. The technical details of both T24 and TD26 will be presented at Chapter 2.

1.4. Manufacturing and Test Process of CLIC Accelerating Structures

The manufacturing and test process of the accelerating structures that are composed of discs includes the steps given below. In this part these steps will be presented.

- RF Design
- Engineering Design
- Ultra Precision Machining
- Quality Control at CERN
- Chemical Cleaning

- Preliminary RF Check
- Diffusion Bonding of Disc Stack
- Assembly of Couplers,Tuning Studs and Cooling Circuits (brazing, machining)
- Tuning of Structure
- Baking (Vacuum 650 $^\circ C$, 3 days)
- High Power Tests
- Post Mortem analysis

1.4.1. RF Design

In order to manufacture the accelerating structure, the first step is the RF design of it. During this step the required parameters such as operating frequency, gradient, phase advance and many other parameters are taken in to consideration. The design in Figure 1.11 is done using HFSS [11].

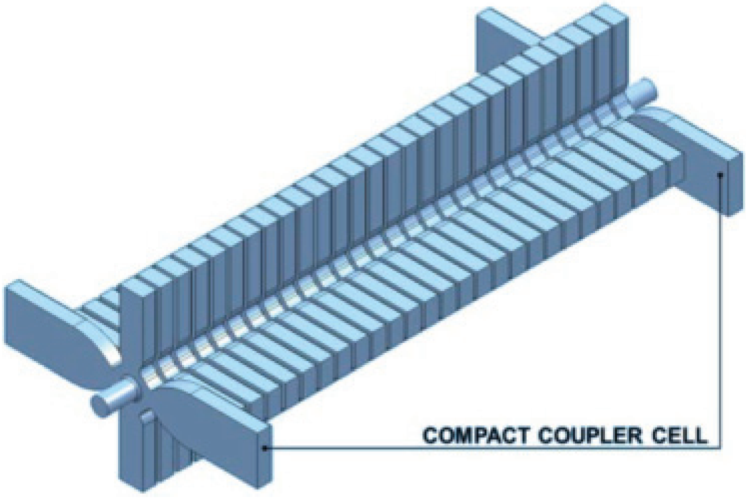

Figure 1.11. RF Design of The Accelerating Structure

1.4.2. Engineering Design

After the RF modelling of the accelerating structure, the next step is engineering design of it. This work includes the designing the metal parts of the structure both disc model that covers the RF part, cooling parts and input/output coupler parts. After this mechanical design, this step also includes the thermal and stress analysis of the structures in order to analyse the mechanical strength of the structure. The design is done using CATIA [12] and ANSYS [14].

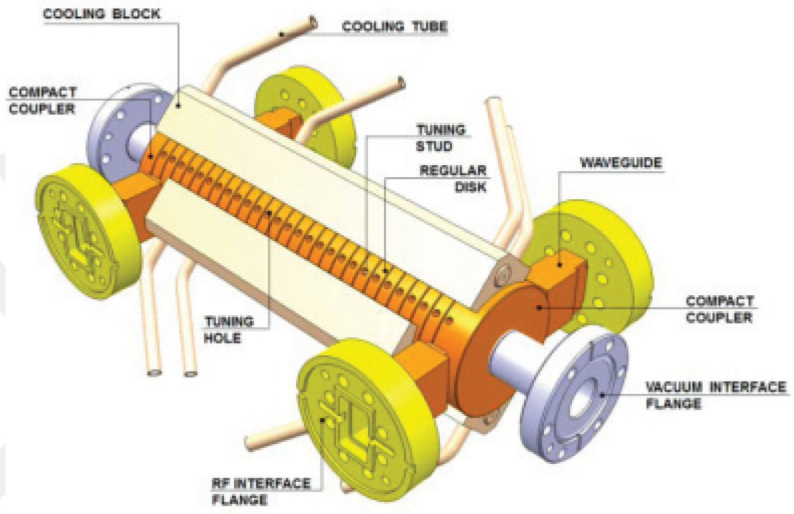

Figure 1.12. Engineering Design Completed Accelerating Structure in 3D Model

1.4.3. Ultra Precision Machining

This step follows the mechanical design of the accelerating structures, the discs that covers the RF part have to be manufactured precisely. The machine considered by the CLIC Study contains a large amount of accelerating structures and individual frequency tuning would be very costly and time consuming. The structures need to be manufactured with enough precision that allows operating without tuning process. They should not include any deformations like scratches, oxidation marks in the RF part especially because of breakdown limitation of the structures (3.10-7 /pulse/m). In CLIC study, the desired precision is 1 μm on the inner radius of the discs according to beam dynamics considerations. This work is also one of the key technologies that CLIC study aims to improve.

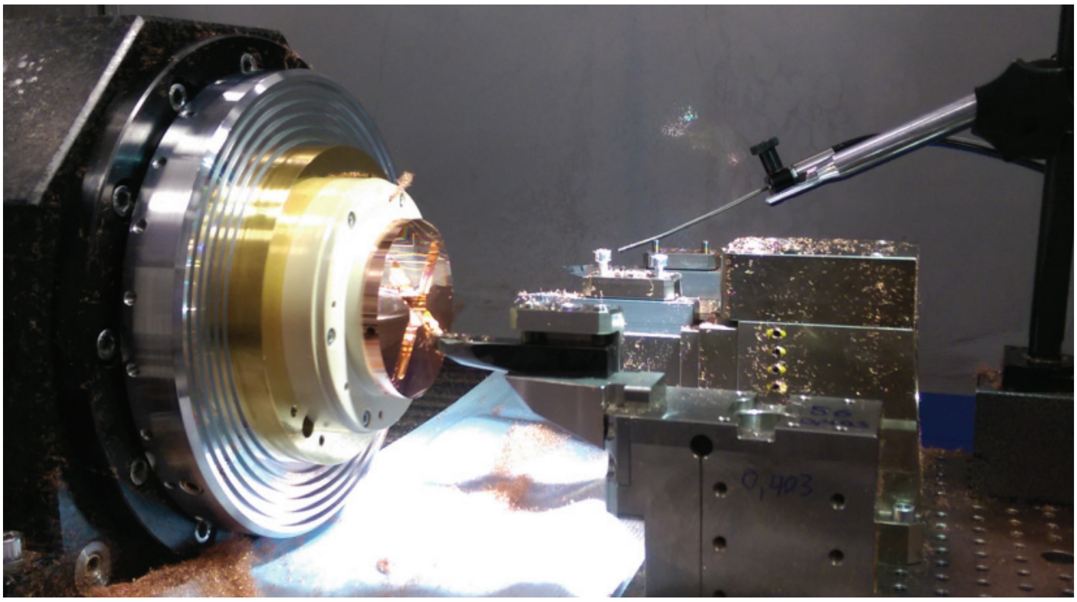

Figure 1.13. Disc at Machining

1.4.4. Quality Control at CERN

After completing the machining of the discs, both the technical drawing parameters and manufactured disc dimensions have to be checked at CERN. This work aims to understand the quality of the machining process by comparing the tolerance values of the design and the tolerance values obtained from company that is responsible for the machining process. CERN Metrology Centre is responsible for this step with the double checking by Coordinate Measurement Machine. This measurement includes several steps; flatness/roughness check, waveguide profile check, iris profile check and all dimensional checks. In this quality control step the machining marks on the discs especially on the RF side must be inspected also with microscopes that have high resolution. The discs may have milling marks in turning area, burrs in sharp edges, damages on external diameter, visible indents/caverns in RF area and all the other foreign materials have to be inspected and reported.

1.4.5. Chemical Cleaning

When the quality control of the discs finished, the next step is cleaning of the discs. This process should be applied to the components that will be operated under vacuum or ultra-high vacuum. The cleaning process aims to remove the thin oxide layer from the surface of the copperas well as any potential pollution. The cleaning process includes steps both chemical solutions and ultrasound techniques. CERN TE-VSC surface treatment workshop is responsible for this process with required equipment and competence [15].

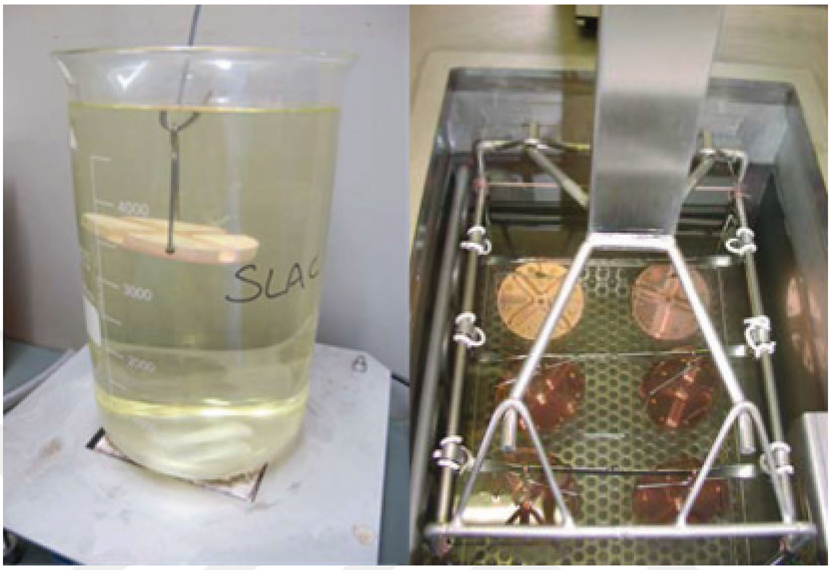

Figure 1.14. Discs at Cleaning Process

The steps of the cleaning process are as follows;

1. Receiving the components, unpacking and visual inspection of the surfaces.
2. Removing the scotch tape and ink traces with a cloth soaked in ethanol or acetone.
3. Arranging a suitable support to hold the components (hook, rod, basket)that avoids contact between them otherwise they can cause surface damage.
4. Degreasing by immersion with detergent NGL Cleaning Technology 17.40 spec. ALU III at 45- 55 $^{\circ}C$ (duration 1-3 h) and ultrasound agitation (10-20 minutes with higher than 40 kHz repetition frequency).
5. Rinsing with water jet followed by immersion.
6. Wettability test with tap or demineralised water.
7. Pickling (de-oxidation) with hydrochloric acid (HCL) in 50% concentration at room temperature for 10 to 20 seconds.

8. Rinsing with demineralised water jet by immersion.
9. Passivation with concentration of chromic acid (H_2CrO_4) 70-80 gr/l and sulphuric acid (H_2SO_4) 3 ml/l at room temperature for 10-20 seconds immersion time.
10. Rinsing with demineralised water jet by immersion.
11. Check the surface. In case of heavily oxidised surface, proceed with step 12 (bright dipping), otherwise proceed with step 14 (final rinsing).
12. Bright dipping in a mixed acids solution with concentration of sulphuric acid (H_2SO_4) 420 ml/l, nitric acid (HNO_3) 80 ml/l and hydrochloric acid (HCL) 2 ml/l at room temperature for 5-10 seconds immersion time.
13. Rinsing with demineralised water jet by immersion.
14. Final rinsing with a demineralised water jet by immersion with or without ultrasound agitation.
15. Spraying with ethanol to facilitate the subsequent drying.
16. Drying in nitrogen or filtered compressed air flow with particular attention to the zones that are prone to retain liquids.
17. Bake by hot air flow at 60 °C for 10 to 60 minutes.
18. Parts shall be left in a clean place to cool down to room temperature.
19. Packing of the components.

1.4.6. Preliminary RF Check

This step aims to understand if the manufactured structure has the RF parameters that are compatible with RF design. These RF test includes; S-parameter measurements that gives the reflection and transmission coefficients of the structure and bead-pull measurements that will be presented in Chapter 4. These tests must be done both before and after the bonding process to compare the design parameters. Also, after high power test, RF tests are important to get information about to how the structures are affected and changed. S-parameter Measurements; S-parameter is the abbreviation of scattering parameters. These parameters can be formed as a square matrix that gives reflection and transmission coefficients of the ports of the structure. These coefficients can be represented as both complex and in decibels. The dimension of the matrix is identified by the number of ports that structure has. S-parameter matrices for 2-port and 4-port networks are given in 1.13 and 1.14 respectively.

$$\begin{bmatrix} S_{11} & S_{12} \\ S_{21} & S_{22} \end{bmatrix} \tag{1.13}$$

$$\begin{bmatrix} S_{11} & S_{12} & S_{13} & S_{14} \\ S_{21} & S_{22} & S_{23} & S_{24} \\ S_{31} & S_{32} & S_{33} & S_{34} \\ S_{41} & S_{42} & S_{43} & S_{44} \end{bmatrix} \tag{1.14}$$

The calculation of these parameters is based on the ratio of the incident and reflected wave voltage amplitudes of the ports that desired to be measured. V$_{N+}$ describes the amplitude of voltage incident wave on port N and V$_{N-}$ describes the amplitude of voltage reflected wave from port N. The scattering matrix [S] can be defined by the form given below in terms of incident and reflected waves [10].

$$\begin{bmatrix} V_1^- \\ V_2^- \\ \vdots \\ V_N^- \end{bmatrix} = \begin{bmatrix} S_{11} & S_{12} & \dots & S_{1N} \\ S_{21} & & & \vdots \\ \vdots & & \ddots & \\ S_{N1} & \dots & & S_{NN} \end{bmatrix} \begin{bmatrix} V_1^+ \\ V_2^+ \\ \vdots \\ V_N^+ \end{bmatrix}, \tag{1.15}$$

In short form;

$$[V^-] = [S][V^+] \tag{1.16}$$

The desired S-parameter can be calculated as;

$$S_{ij} = \left. \frac{V_i^-}{V_j^+} \right|_{V_k^+=0 \; for \; k \neq j} \tag{1.17}$$

The measurement of S-parameters is being done by a device called Vector Network Analyzer as illustrated in the figure. Usually there are two kind of VNA; 2-port VNA and 4-port VNA. They also have different capabilities (working frequency, bandwidth, resolution) and technical properties. By clamping input/output coupler parts, the structure has ports to get a connection with VNA (Vector Network Analyzer) and ready for the RF tests.

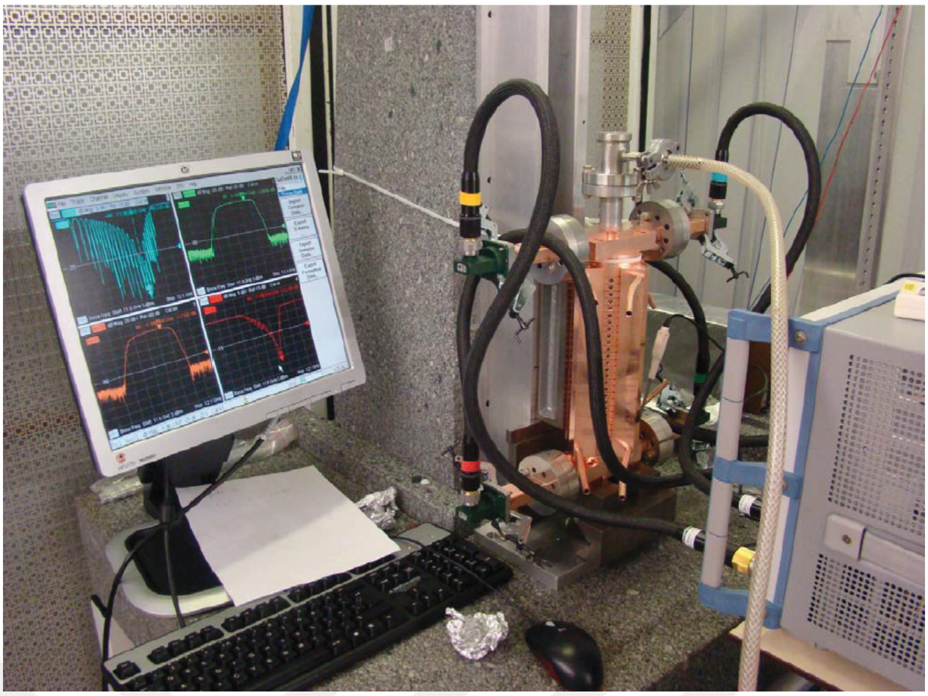

Figure 1.15. Accelerating Structure at RF Check

1.4.7. Diffusion Bonding of Disc Stack

If the preliminary RF check step is compatible with the RF design, the next process diffusion bonding can start. This step is basically assembling the disc stack in a furnace by applied pressure and heating. Actually the assembling of the linacs can be carried out by brazing but only the linacs operating in L (1-2 GHz), S (2-4 GHz) and C (4-8 GHz) frequency bands. For the X Band (8-12 GHz), diffusion bonding has been used in order to obtain better contact. This process is done by heating the contacting surfaces of the discs in a bonding furnace about 1000 °C. During the heating, the connection parts of the discs must be kept under pressure [16].

The CLIC diffusion bonding requirements [17];

- Temperature, 1030 °C
- Time, 1.5 h
- Vacuum,10_{-5}-1_{0-6} mbar
- H_2 partial pressure, 20 mbar
- Applied pressure on the top disc, 0.1 MPa

- Thermocouples connected to the structure body
- Witness disc (for further pollution analysis)

Figure 1.16. Outside and inside view of bonding oven [17]

1.4.8. Assembly of Couplers, Tuning Studs and Cooling Circuits

When the bonding of the disc stack finished, the other parts must be assembled to complete the full structure. This step includes the brazing of the input and output power couplers, tuning studs and cooling circuits of the accelerating structure. Input/output coupler parts have different geometry as compared to regular accelerating discs and they are being used for supplying the RF power inside the structure (inputs) and transferring the RF power along the structure to the outputs that have an external load to suppress the power. Tuning studs are used in order to set the frequencies of the individual cells of the structure to the desired operating frequency. The cooling circuits are one of the critical components to stabilise the operating frequency of the structure by keeping the structure temperature under control. The usual assembly technique of these parts is brazing. The brazing is a process that is being used for joining metal structures to each other. It includes the usage of filler materials between the connection of the metal structures and a brazing furnace to heat the filler material to complete the process. The brazing furnace provides heat for melting the filler material that is getting solid after the process when structures are joined. The filler material can be the same as structure material (copper) or an alloy and it can be in the form of brazing foil or a brazing wire. While the brazing process the connection part is heated to a certain temperature that is lower than the melting point of the metal parts but high enough to melt the filler material. Then cooling cycle of the process the filler material solidifies and creates a strong connection at the brazing joint. In CLIC study, used filler materials are Cu-Ag, Cu-Au and Ag-Pd for brazing.

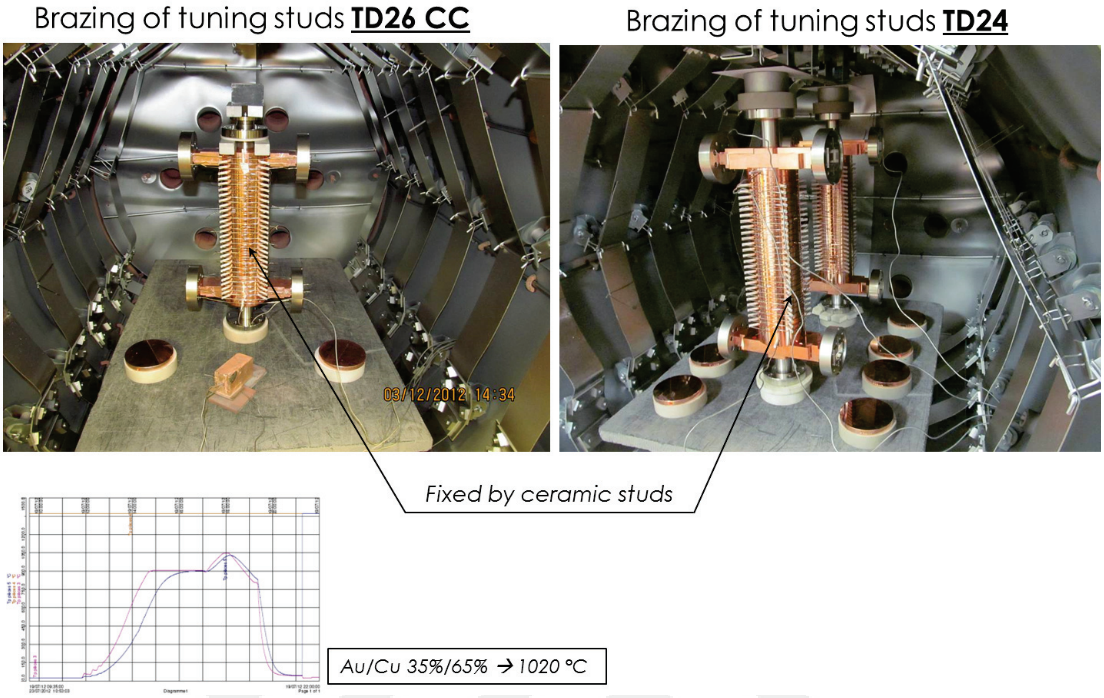

Figure 1.17. Couplers and tuning studs are under brazing process [17]

1.4.9. Tuning of The Structure

During the bonding and brazing process, deformations can change the inner volume of the cavity. This causes a frequency change inside the cavity. To overcome this problem, individual cells must be tuned after the joining process to obtain the nominal operating frequency of the accelerating structure. The tuning process can be conducted with the help of a computer program that shows the changes of the frequency by taking the instantaneous data from the Vector Network Analyser (VNA). In order to set the frequency of the individual cells up and down, tuning studs must be assembled on to the discs that described at the previous section. Then, a special hammer can be used to set the frequencies by pushing or pulling the pins, so decreasing and increasing the cell volume, the cavity frequency can be set upper or lower, respectively. During this process the temperature of the room and humidity should be taken into account. The temperature change for the the linacs operating at X-Band frequency range (operating at 12 GHz) is

200 kHz/°C. 1 °C increasing in temperature causes 200 kHz decreasing of the frequency, vice versa. The sensitivity of the operating frequency of the linac depends on its design and operating frequency band. Humidity inside the cavity can also change the operating frequency of the linac, for instance the dielectric constant of air at 20 °C and 60 % humidity is approximately 1.0006 that can lower the frequency by 0.3% from its value in vacuum. To overcome the humidity, nitrogen can be applied into the structure [16].

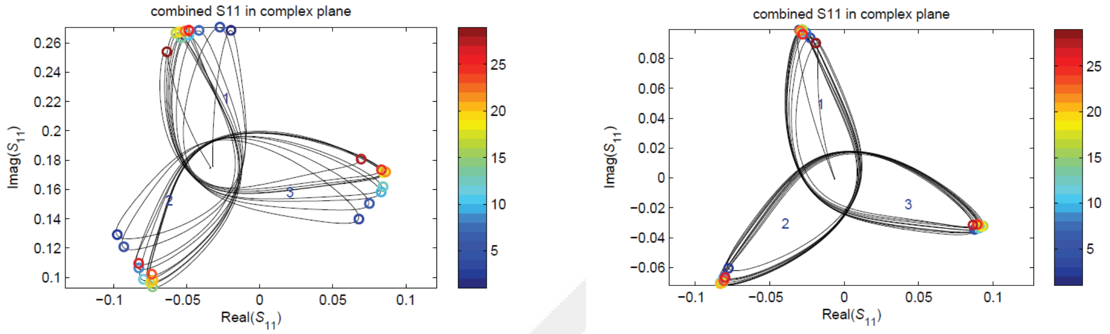

Figure 1.18. S_{11} of structure TD26 in complex domain before (left) and after (right) tuning

1.4.10. Baking

Also, during the bonding process because of the usage of H_2, the structure has H_2 inside. The aim of baking process is providing a thermal energy to absorbed gas molecules both on the surface and absorbed inside the inner surface to release them. This process needs a furnace that has both heating and vacuum capability [16].

CLIC study accelerating structures have the baking requirements given below [17];

- Temperature 650 °C
- Vacuum 10^{-9} mbar
- Duration 3 days (at least)

1.4.11. High Power Test

High power tests of the accelerating structures are one of the main research topics of CLIC Study. The accelerating structures work at very high electric fields and tend to breakdown frequently even under vacuum. The produced structures are being tested in the X band klystron based test stands at CERN. This test includes applying the RF power to the structure to reach an unloaded gradient 100 MV/m by increasing the applied power gradually while keeping the breakdown rate under control, in CLIC Study BDR $3x10^{-7} pulse^{-1} m^{-1}$ when beam loading is in consideration [5]. This process called RF conditioning. The duration of the test is depending on the structure RF design and it can take few months to be completed. As an observation, the structures that have been designed with damping parts take more time to complete the high power test compared to the other structures that have no damping part inside [19].

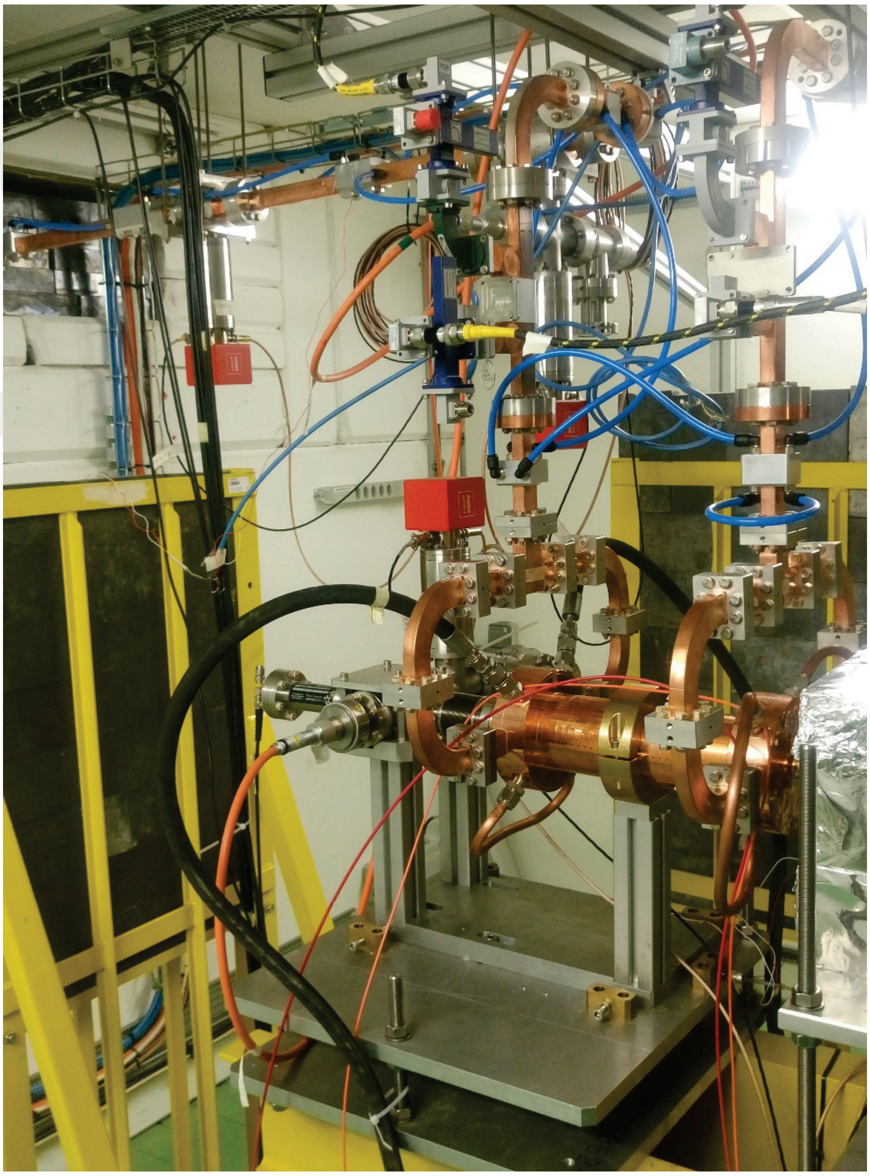

Figure 1.19. X-Band Accelerating Structure is at High Power Test

1.4.12. Post Mortem Analysis

The completion of the high power test of the structures follows the next and last step; post mortem analysis. This process includes the endoscopy of the structure; observing inside of the structure by a small camera and according to this observation and the data taken during high power tests, deciding how and which parts of the structure will be cut to observe the breakdown regions. RF measurements (S-parameter and bead-pull) of the structure after high power test are also included in this last step work to understand how the electric field profile inside, the operating frequency and phase advance of the cells has changed. The cutting process of the structures depends on the parts of the cells that have undergo breakdown. Because of this, there is no distinct procedure for the cutting process of them. The cutting process has to be decided according to information from the endoscopy and RF measurements after high power test.

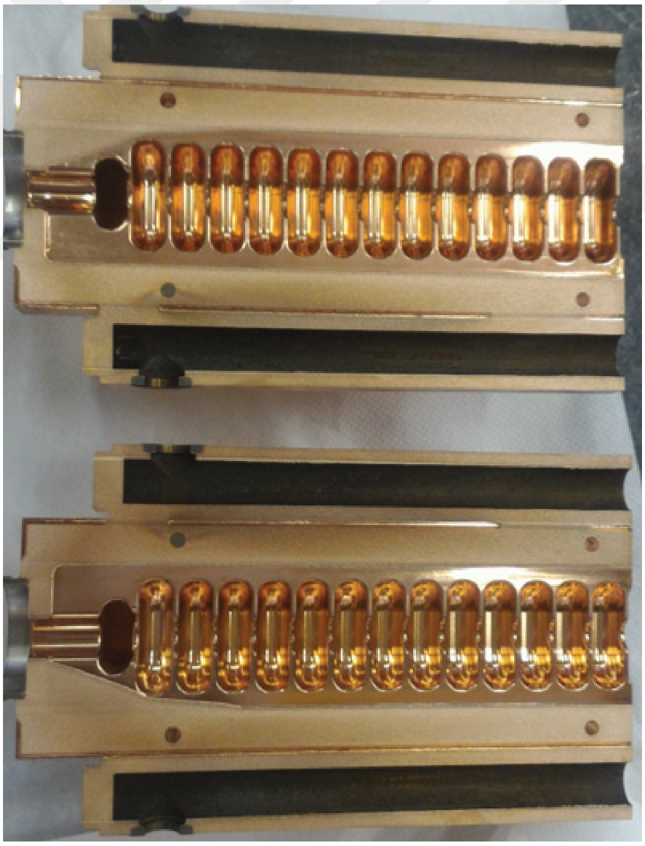

Figure 1.20. Parts of the X-Band Structure After Cutting Process [13]

1.5. Motivation of Thesis

Manufacturing expense of the accelerating structures accounts for approximately a fourth of the cost of the LINAC as the manufacturing process includes many steps as described previous sections. All the steps have an importance and very tight tolerances to obtain the required CLIC parameters. Among all the manufacturing steps, both machining and bonding are more critical compared to other steps according to tolerances. CLIC requires precise machining with shape accuracy ±2.5 μm and 25 nm roughness as illustrated in Figure 1.21 and alignment controlled symmetrical heating for bonding to overcome possible bending and shape defects of the structure as shown in Figure 1.22.

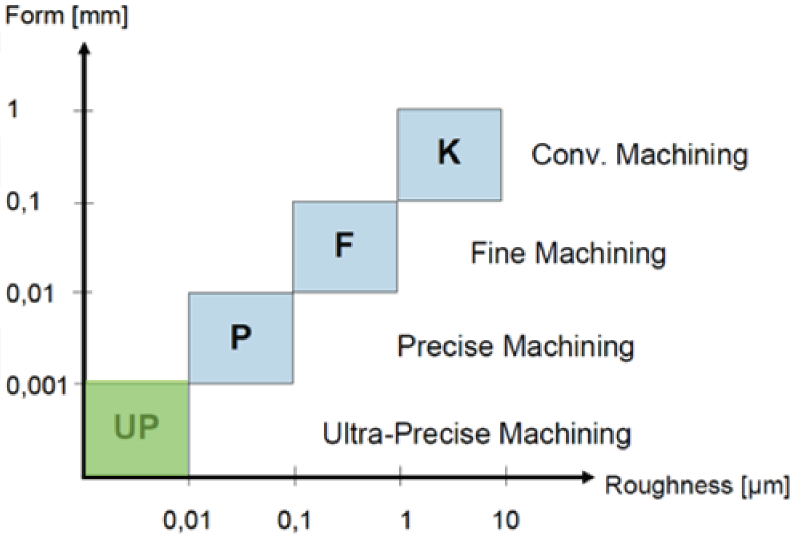

Figure 1.21. Classification of the machining process according to tolerances of shape accuracy and roughness [18]

The aim of this study is to investigate a potential geometrical correlation between the frequency deviations and geometrical imperfections of the individual discs of the accelerating structures before and after bonding process to understand how bonding process affects the geometry of the discs or else, how the final performance of the structure is defined by the machining process of the discs. According to the results of this study, the manufacturing process can be optimised and the effects of the bonding on the quality of the discs can be understood. In this thesis, the design and features of the main accelerating structures (T24 and TD26) with HFSS simulations will be presented in Chapter 2. The methodology including inner parameter dimension measurements and bead-pull method for the cell frequency changes will be described in Chapter 3. Then the results

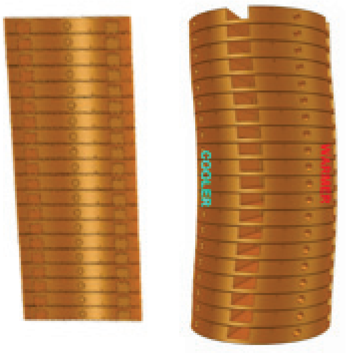

Figure 1.22. Shape deflection caused by unbalanced weight and asymmetrical heating during bonding [17]

and conclusions will be presented in Chapter 4 and 5 respectively.

CHAPTER 2

STRUCTURES AND SIMULATIONS

In the process of the designing accelerating structures, there are important figures of merit that need to be taken into account. In this chapter, the technical details of both T24 and TD26 are presented with a special mention to their figures of merit. Simulations were made to evaluate the sensitivity of the frequency to the geometrical parameters of the discs.

2.1. Operating Frequency

Operating frequency is the basic parameter that defines an accelerator structure. The availability of RF power sources is key on the final decision of the operating frequency. But the frequency also affects many other parameters as shown in Table 2.1 where the appropriate scaling are also indicated.

Table 2.1. Dependency of parameters to the frequency

Shunt Impedance	Quality Factor	Total Peak Power
$Z_0 \sim f^{1/2}$	$Q \sim f^{-1/2}$	$P_{tot} \sim f^{-1/2}$
RF Energy Stored	Power Filling Time	Minimum Energy Stored
$U \sim f^{-2}$	$t_F \sim f^{-3/2}$	$Z_s/Q \sim f$

2.2. Accelerating Voltage

This term represents the axial voltage available to accelerate the particles through the structure from input to output and can be determined by the formula 2.1 (where L is the length of structure in the propagation of direction z).

$$V_{acc} = | \int_0^L E_z(z) e^{j\omega z/c} dz| \tag{2.1}$$

2.3. Gradient

Gradient describes the average electric field gained by a charged particle in an accelerating structure. It is expressed in nominal units (MV/m) and the formula 2.2.

$$E_{acc} = \frac{|V_{acc}|}{L} \tag{2.2}$$

2.4. Quality Factor

Quality factor is described by the formula 2.3 where ω_0 , U, P_{loss} represents the operating frequency, stored energy and power loss in structure walls. Quality factor represents the capacity of the device to storage energy.

$$Q_0 = \frac{\omega_0 U}{P_{loss}} \tag{2.3}$$

2.5. Phase Advance

This term describes the phase difference between the adjacent cells of the traveling wave accelerating structures and can be computed from the formula 2.4 given below where D and k_0 represent the distance between the loaded discs inside the structure and axial wavenumber of the electromagnetic signal respectively.

$$\triangle\phi = k_0 D \tag{2.4}$$

2.6. Filling Time

The filling time describes the time required for the electromagnetic field to fill the accelerating structure and it can be calculated by dividing the whole length of the structure by the group velocity.

$$t_F = \frac{L}{\upsilon_g} \tag{2.5}$$

2.7. Phase Velocity

Phase velocity is the velocity of electric field pattern inside the structure and is represented by the formula 2.6 where ω and *k* represents the frequency and wave number. This velocity can be calculated from the dispersion curve of the disc loaded structure at the desired operating frequency.

$$\upsilon_{ph} = \frac{\omega}{k} \tag{2.6}$$

2.8. Group Velocity

Group velocity describes the velocity of the energy flow inside the structure and represented as the formula 2.7 where U and P_{in} represents the energy and input power respectively. This velocity can be calculated from the derivative of the phase velocity from the dispersion curve at the same operating frequency.

$$\upsilon_{g} = \frac{P_{in}}{U} \tag{2.7}$$

$$\upsilon_{g} = \frac{\mathrm{d}\omega}{\mathrm{d}k} \tag{2.8}$$

2.9. Shunt Impedance

The shunt impedance qualifies the efficiency of the accelerating structure. The higher the value, the larger the obtainable accelerating voltage for a given applied power. It is expressed in ohm (Ω) unite and by the formula 2.9.

$$R = \frac{(V_{acc})^2}{2P_{diss}} \tag{2.9}$$

2.10. CLIC Structures

In this work, two accelerating structures were used T24 and TD26. They are both constant gradient traveling wave structures that operate at 12 GHz and are designed for

100 MV/m unloaded gradient. Both structures are tapered which means the structure shape is getting narrower from input to output to decrease the group velocity.

2.10.1. T24 Accelerating Structure

The T24 is a constant gradient tapered structure composed of 24 accelerating cells, compact input and output couplers for RF power transfer, as illustrated with the RF design and mechanical design (Figure 2.1 and Figure 2.2 respectively). For T24 abbreviation, ’T’ means ’traveling wave’, 24 describes the number of regular discs of the structure.

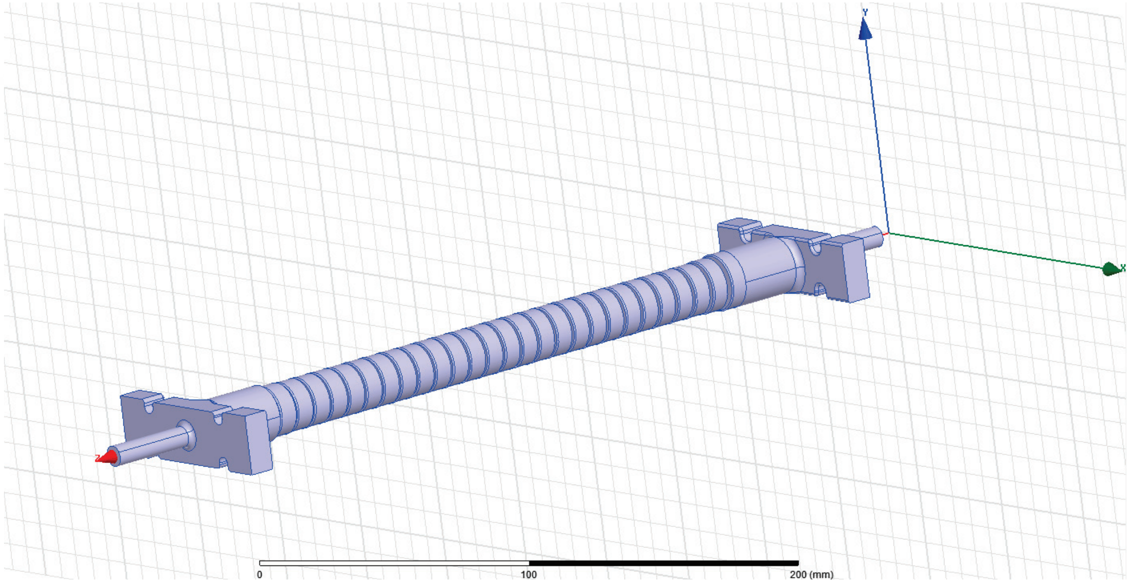

Figure 2.1. T24 RF Design in HFSS

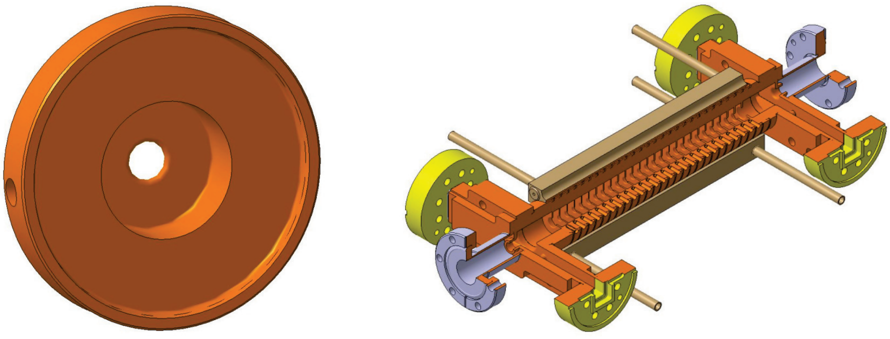

Figure 2.2. 3D Mechanical Model of T24 cell and accelerating structure

The T24 was designed for 11.9942 GHz operating frequency at 30 °C temperature with $2\pi/3$ phase advance per cell. The material of T24 is Cu (OFE) C10100 that stands for oxygen-free electronic copper and includes 99.99% pure copper and 0.0005% oxygen. The mechanical design was done using CATIA V5 R23 Mechanical design software.

Table 2.2. Table of parameters for T24 [20]

Parameter	T24
Quality Factor	6815
Filling Time, t_F (ns)	57.25
Group Velocity input/output (%c)	1.815/0.917
Iris Radius input/output (mm)	3.15/2.35
Structure Length (Regular cells) (mm)	200
Whole Structure Length (mm)	227.5
Input Power (MW)	42.2

2.10.2. TD26 Accelerating Structure

The TD26 is a constant gradient tapered structure composed of 26 accelerating cells, compact input and output couplers for RF power transfer, as illustrated with an RF design and mechanical design Figure 2.3 and Figure 2.4 respectively. The disc design of TD26 has four waveguide parts around the main RF part for higher order mode damping. For TD26 abbreviation, 'TD' means 'traveling wave damped' and 26 describes the number of regular discs of the structure.

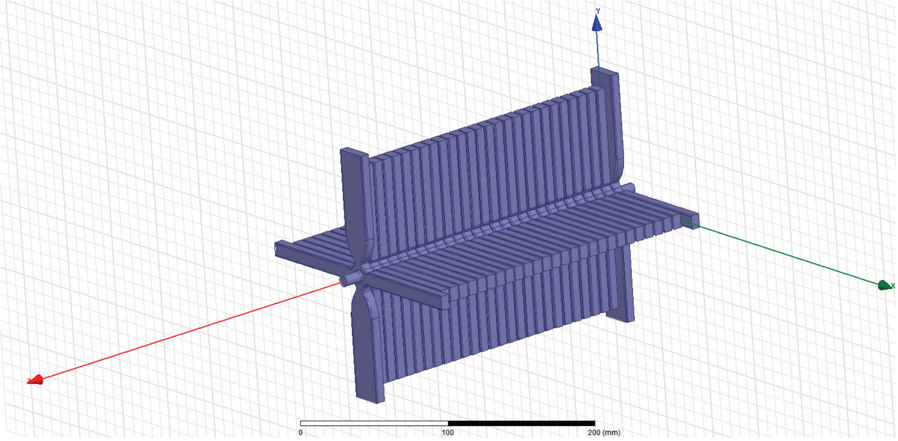

Figure 2.3. TD26 RF Design in HFSS

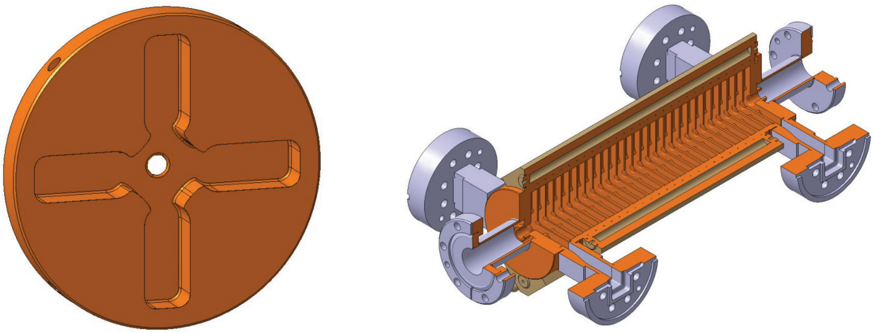

Figure 2.4. 3D Mechanical Model of TD26 cell and accelerating structure

The TD26 was designed for 11.9942 GHz operating frequency at 30 °C temperature with $2\pi/3$ phase advance per cell. The material of TD26 is Cu (OFE) that the same material as T24. Also the mechanical design of TD26 was done by the same software as T24.

Table 2.3. Table of parameters for TD26 [21]

Parameter	TD26
Quality Factor	5843
Filling Time, t_F (ns)	66.27
Group Velocity input/output (%c)	1.698/0.84
Iris Radius input/output (mm)	3.15/2.35
Structure Length (Regular cells) (mm)	216.6
Whole Structure Length (mm)	250
Input Power (MW)	49.3

2.11. Simulations of the Structures

In this section, we present the parametric simulation of T24 and TD26 structures done using ANSYS HFSS electromagnetic design and simulation suite. Parametric studies of both structures were done from the original geometry.

2.11.1. Finite Element Method

The finite element method was developed for structural analysis in mathematical physics. It gives the approximate solutions for complex geometries that can not be solved by hand. The mathematical representation of this method was conducted by Richard Courant in 1943.

In the beginning, FEM had been applied for especially mechanical analysis and modelling problems that had complicated geometries to solve by hand like bridges or aircrafts. The application of FEM to electromagnetic structures started in 1968 for different kind of sub-areas like electric machines, semiconductor devices or microstrip structures.

Finite element method (FEM) is not so easy to program as compared to other electromagnetic analysis methods such as finite difference method (FDM) and method of moments (MOM). FEM is especially effective for both complex geometries and inhomogeneous media. A computer programme which is coded according to FEM principles can easily be used for analysis of the structures in different areas with or without modification [23]. Finite element method includes four main steps;

- Discretizing of the problem region into a finite amount of sub-regions
- Obtaining equations for all sub-regions
- Collecting all the sub-regions in the solution region
- Solution process of the determined equations

The discretization of the problem area means that dividing the full region into sub-regions called finite elements. The finite elements can be one, two or three dimensional as illustrated in the Figure 3.1. The usage of the finite element type depends on the structure shape that is under analysis.

The discretization step affects the storage requirement of the computer, time of computation and accuracy of the results depending on the user selections about mesh type and interpolation equations. FEM gives the approximate solution according to solution region as illustrated in the Figure 2.6.

In order to obtain the equations for all sub-regions, we must be select the interpolation function. This function can be selected in different kind of forms such as trigonometric or polynomial according to structure type. Polynomial functions can also be classified as linear (first), quadratic (second) or higher order polynomials. Using higher order polynomials extend the computation time because of complicated formulation, but it increases the accuracy of the results.

After obtaining the equations for all sub-regions, all of the equations are collected to obtain an approximate solution for the complete region. By applying Ritz variational method or Galerkin's method to these collected equations, the system of equations for

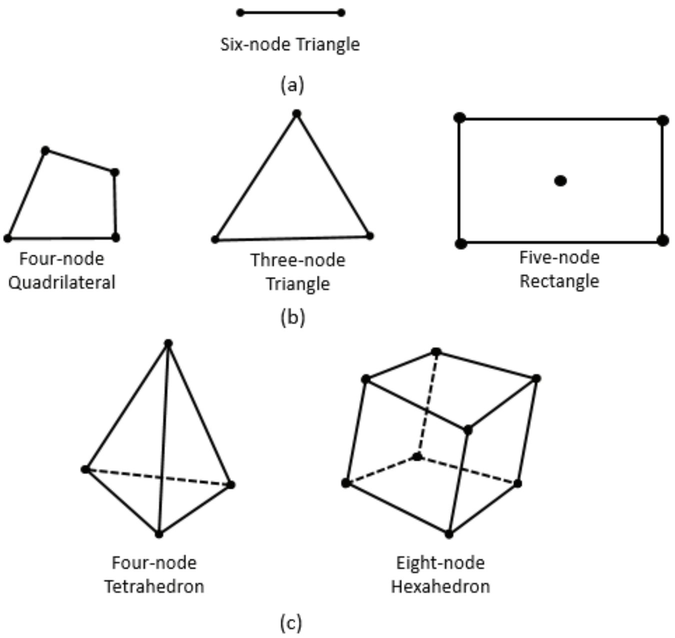

Figure 2.5. Finite elements; a) one-dimensional, b) two-dimensional, c) three-dimensional

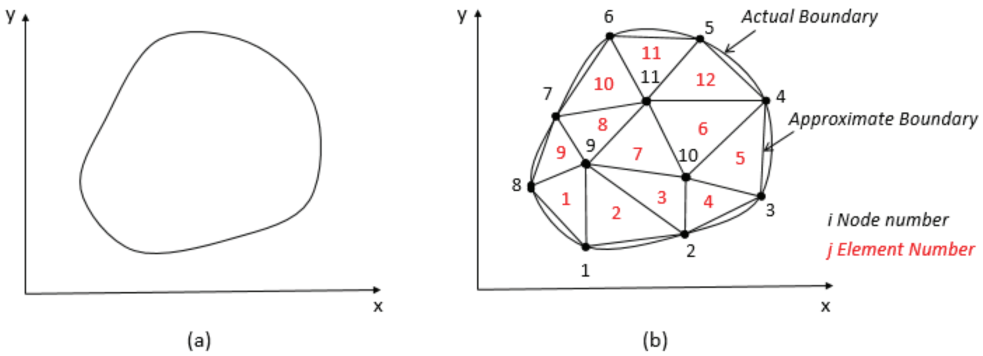

Figure 2.6. a) Solution region, b) Discretization of the solution region

the entire problem region can be obtained and the boundary-value problem of the set of equations can be solved [24].

The last step of FEM is solving the system of equations that has been obtained for the solution region according to boundary conditions (Neumann or Dirichlet) applied to the structure. The equations can be in deterministic form (3.1) where *K* represents NxN symmetric matrix (N describes the total number of nodes), ϕ is Nx1 vector represents the unknown expansion coefficients, b is Nx1 known vector when solution area includes source.

$$[K]\{\phi\} = \{b\} \tag{2.10}$$

The equations can also be in eigenvalue form where *K* can be written as [A]-λ[B] where λ is an eigenvalue. This equation type is valid for source-free solution regions in electromagnetics.

$$[A]\{\phi\} = \lambda[B]\{\phi\} \tag{2.11}$$

After solving the equations for ϕ, the desired parameters and plots can be obtained by post-processing [24].

2.11.2. ANSYS HFSS

ANSYS HFSS (High Frequency Simulation Structure) software was created based on Finite Element Method for numerical computation of the electromagnetic design and analysis. It allows one, two and three dimensional modelling and analysis of the structures that are operating at high frequency. With the usage of other ANSYS packages, it is possible to do the mechanical and thermal analysis of the high frequency structures after electromagnetic design [11].

Modelling and analysing in HFSS follows these steps;

- Decision of the solution type
- Modelling the structure
- Applying excitation ports if necessary
- Applying boundary conditions
- Setting the solution parameters

- Post-processing of the results after simulation finished

HFSS has different kind of solutions according to problem region such as driven modal, driven terminal, transient and eigenmode. In this work, eigenmode was used to analyse the discs to determine the frequency dependency of the geometrical parameters. The phase advance $2\pi/3$ of the discs were imposed by using master-slave property of boundaries. HFSS allows for use of symmetry planes (Perfect H) according to structure shape. In order to reduce the computation time, Perfect H boundary condition was applied to the symmetry axis of the designs as illustrated in Figure 2.7.

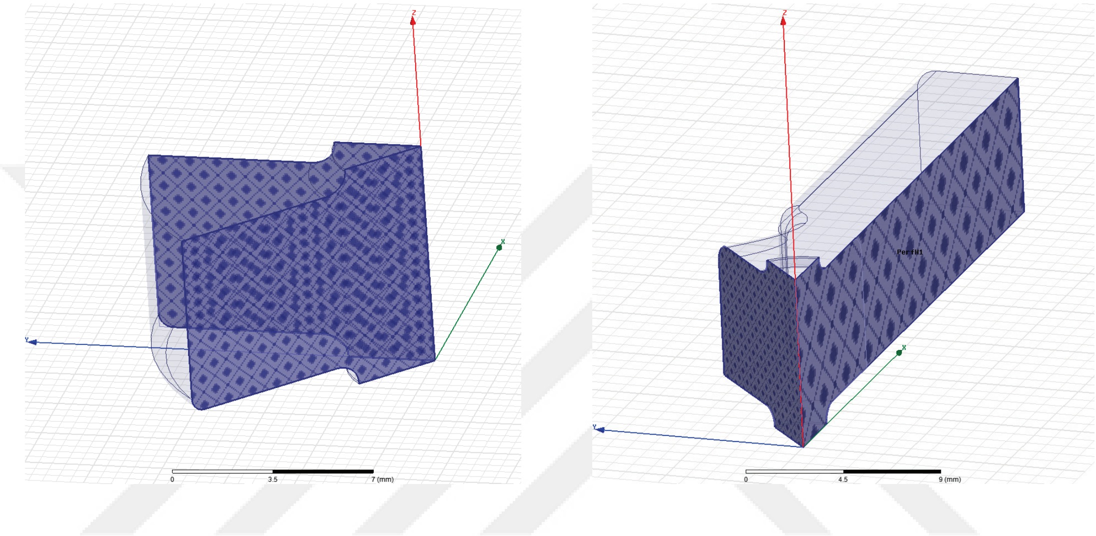

Figure 2.7. Symmetry planes of T24 (left) and TD26 (right) discs

2.11.3. ANSYS HFSS Analysis Results of T24 and TD26 Structures

Parametric simulations of both T24 and TD26 first, middle and last cells were done by varying the geometrical parameters in the range 20 μm with 1 μm steps to determine the sensitivity of every dimensions to the frequency.

2.11.3.1. Geometrical Parameters and Mesh View of T24

Geometrical parameters of T24 is as illustrated in Figure 2.8 below.

The mesh view of T24 cell is shown in Figure 2.9 below. Second order basis functions were used for the analysis. The maximum length of elements were specified as 2 mm and the surface approximation was set as 1 μm on the curvature parts as shown.

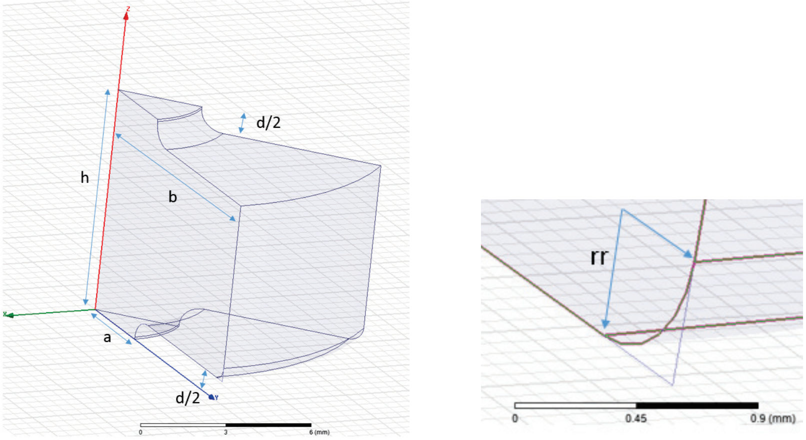

Figure 2.8. T24 geometrical parameters entire disc (left) and bended part (right)

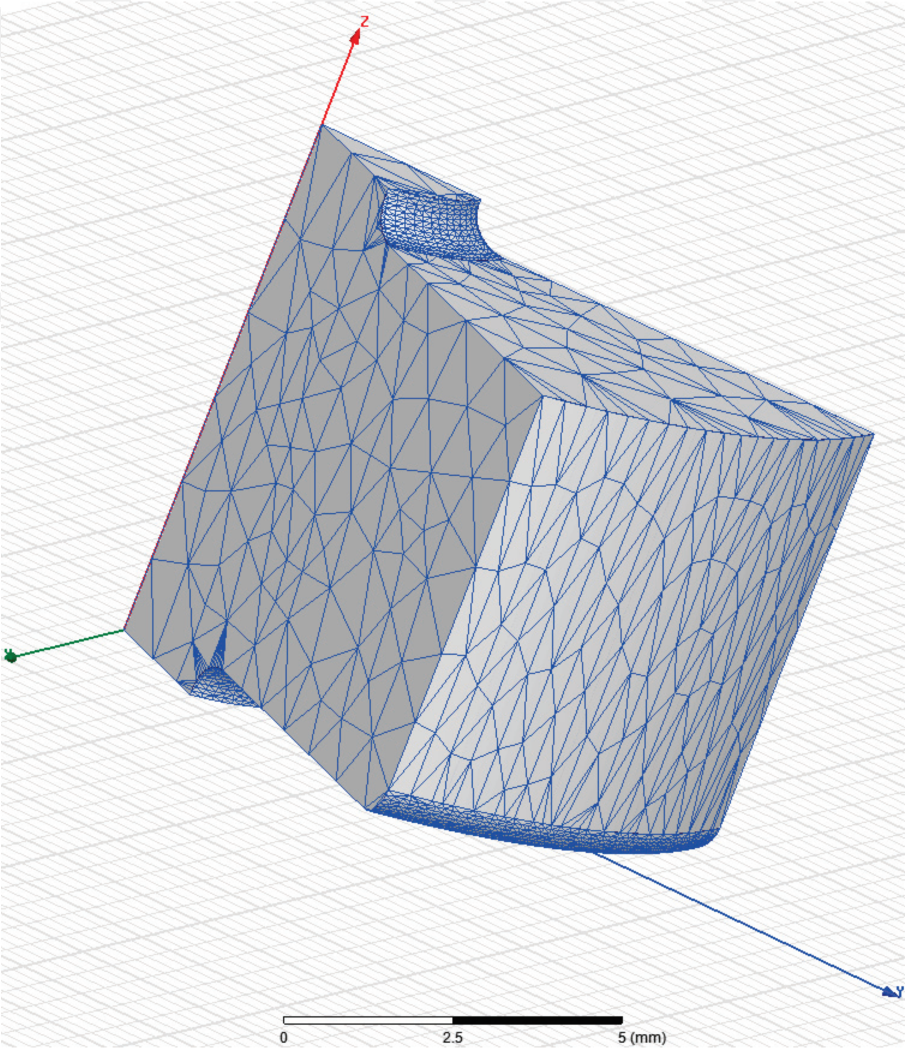

Figure 2.9. Mesh view of T24 cell in ANSYS HFSS

2.11.3.2. Simulation Results for T24

The parametric analysis of the T24 cells RF design were done for first, middle and last cells in ±10 μm range from the nominal value. The nominal design values of T24 cells were given in Table 2.4 for first, middle and last cells respectively.

Table 2.4. Nominal values of T24 First, Middle and Last cells

Parameter	First Cell(mm)	Middle Cell(mm)	Last Cell(mm)
a	3.15	2.75	2.35
b	9.96775	9.8359	9.7356
d	1.67	1.335	1
h	8.332	8.332	8.332
rr	0.5	0.5	0.5

According to simulation results for first, middle and last cells given below, all the parameters have an effect on frequency change, but the most sensitive parameter for frequency change is the inner radius labelled ’b’.

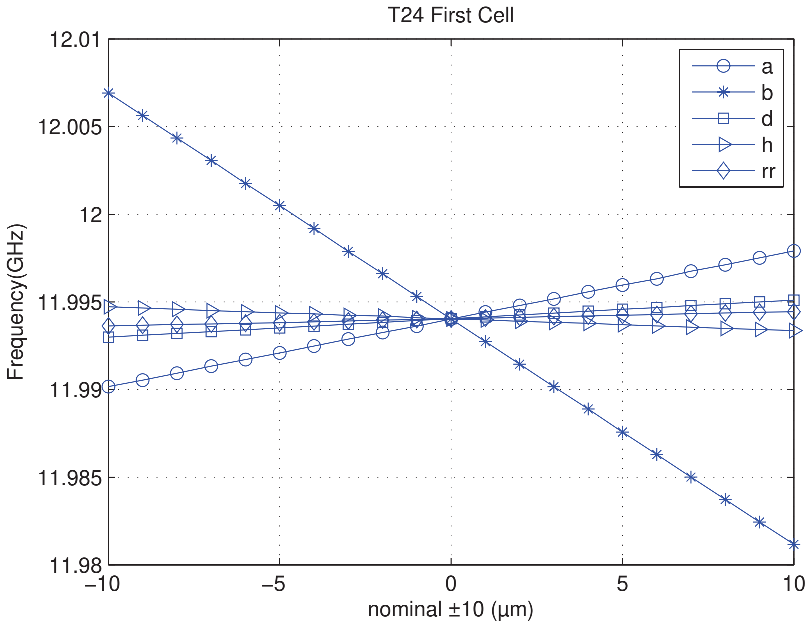

Figure 2.10. Sensitivity comparison of T24 First Cell geometrical parameters

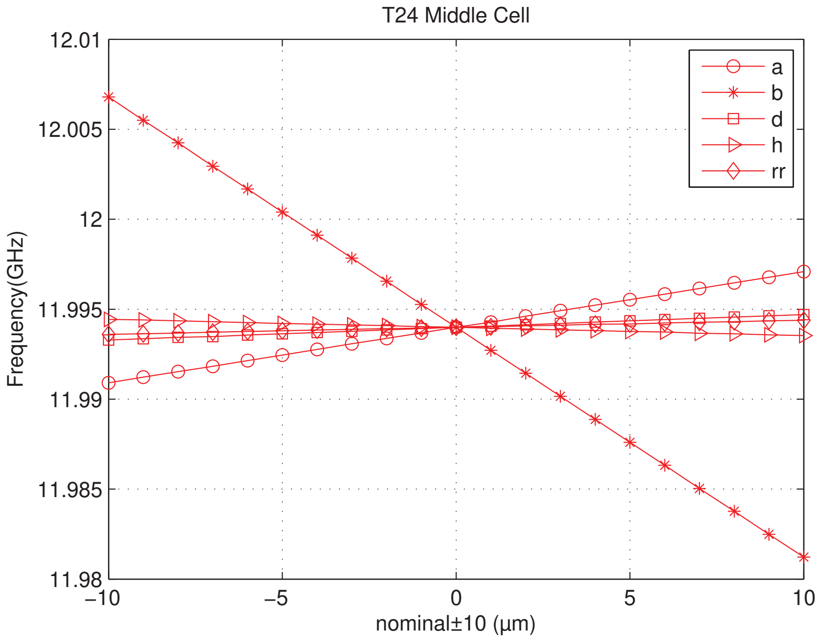

Figure 2.11. Sensitivity comparison of T24 Middle Cell geometrical parameters

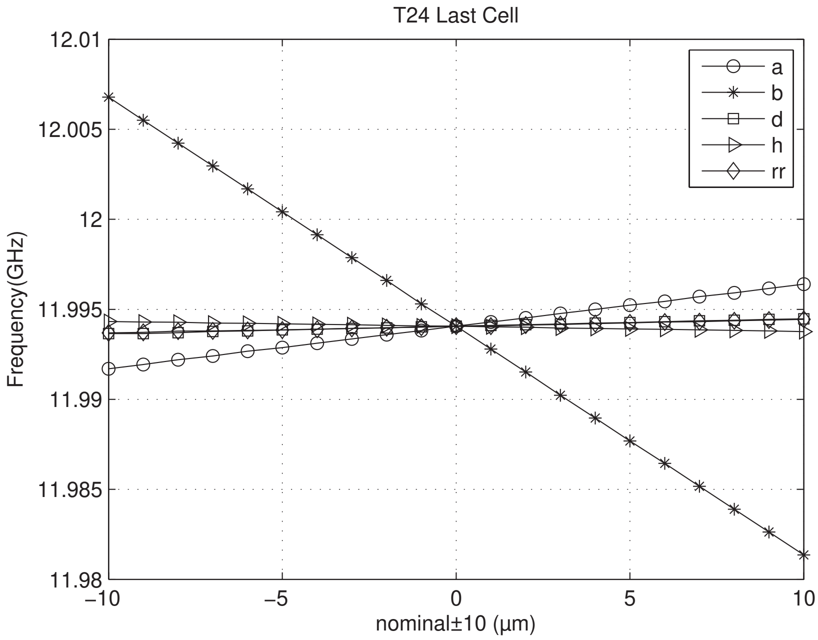

Figure 2.12. Sensitivity comparison of T24 Last Cell geometrical parameters

Table 2.5. Δf for 1 μm change in parameters of T24 cells

Parameter	First Cell(MHz)	Middle Cell(MHz)	Last Cell(MHz)
a	0.387	0.309	0.235
b	1.287	1.278	1.271
d	0.105	0.071	0.041
h	0.069	0.045	0.028
rr	0.041	0.040	0.038

Due to the tapered feature of the T24 structure, the frequency deviation for 1 μm change is also decreasing from input to output as illustrated in Table 2.5.

2.11.3.3. Geometrical Parameters and Mesh View of TD26

Geometrical parameters of TD26 illustrated in Figures 2.13, 2.14 and 2.15. RF design of TD26 is more complex compare to T24 and it also uses equations to define some parameters.

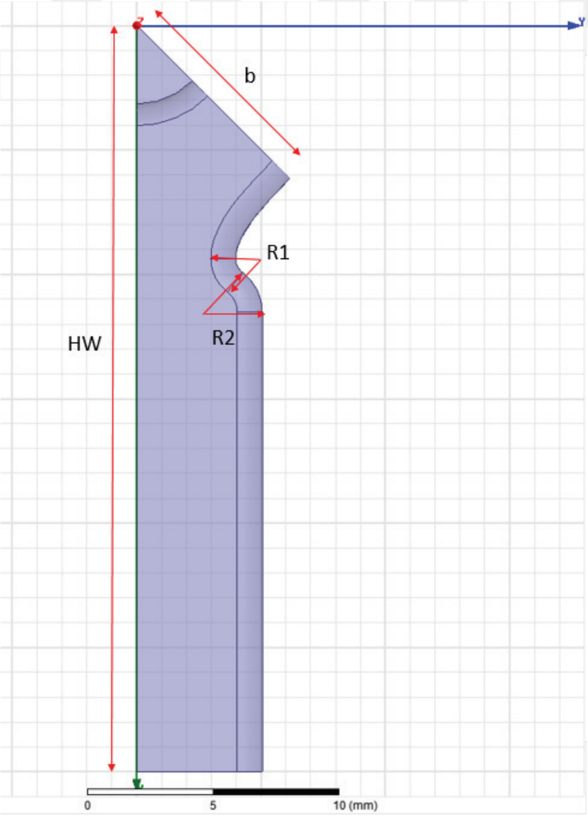

Figure 2.13. TD26 Geometrical Parameters (view on top)

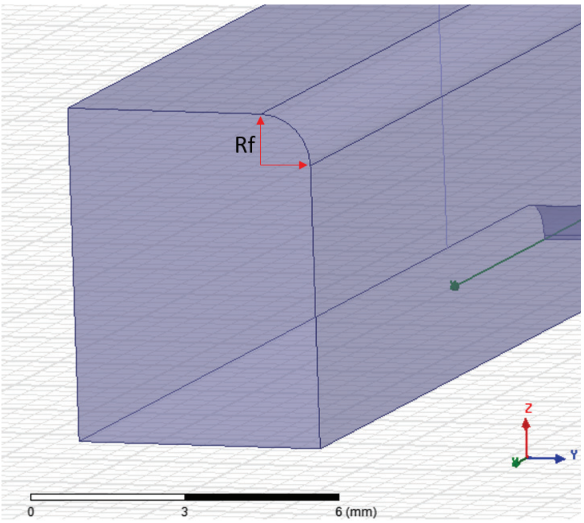

Figure 2.14. TD26 Geometrical Parameters (bended part)

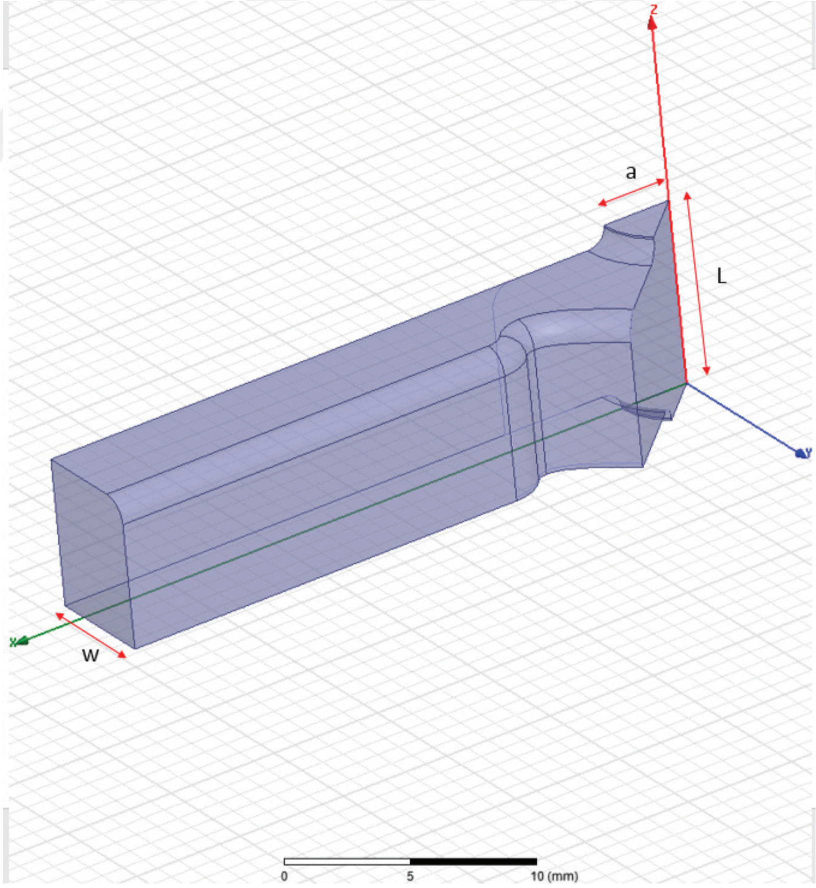

Figure 2.15. TD26 Geometrical Parameters (view on side)

The mesh view of TD26 cell is shown in Figure 2.16 below. Second order basis functions were used for the analysis. The maximum length of elements were specified as 0.3 mm and the surface approximation was set as 5 μm on the curvature parts as shown.

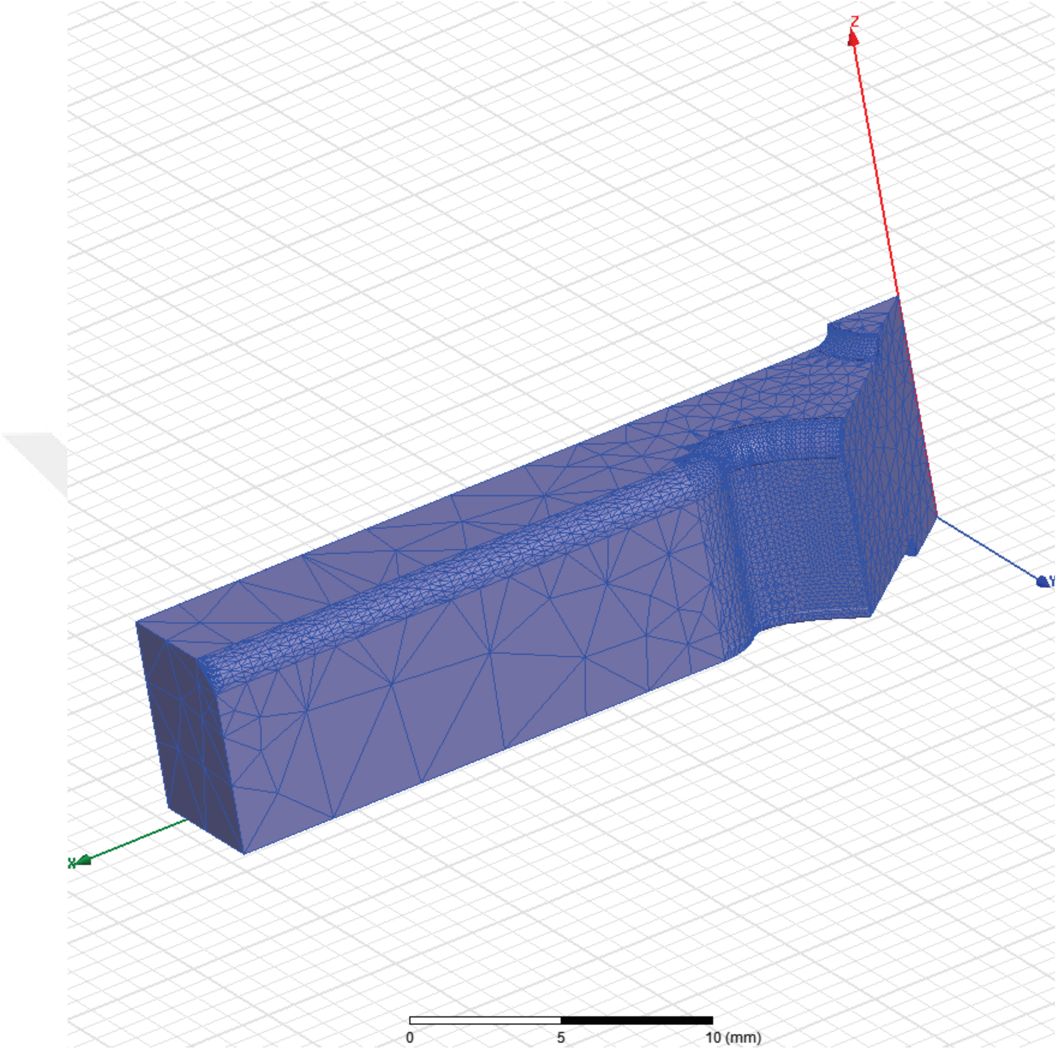

Figure 2.16. TD26 Mesh View

2.11.3.4. Simulation Results for TD26

The parametric analysis of the TD26 cells RF design was done for first, middle and last cells within ±10 μm range from the nominal value. The nominal design values of TD26 cells are given in Table 2.6 for first, middle and last cells respectively.

As seen from the simulation results for first, middle and last cells below, the most sensitive parameter is the inner radius for frequency change(b).

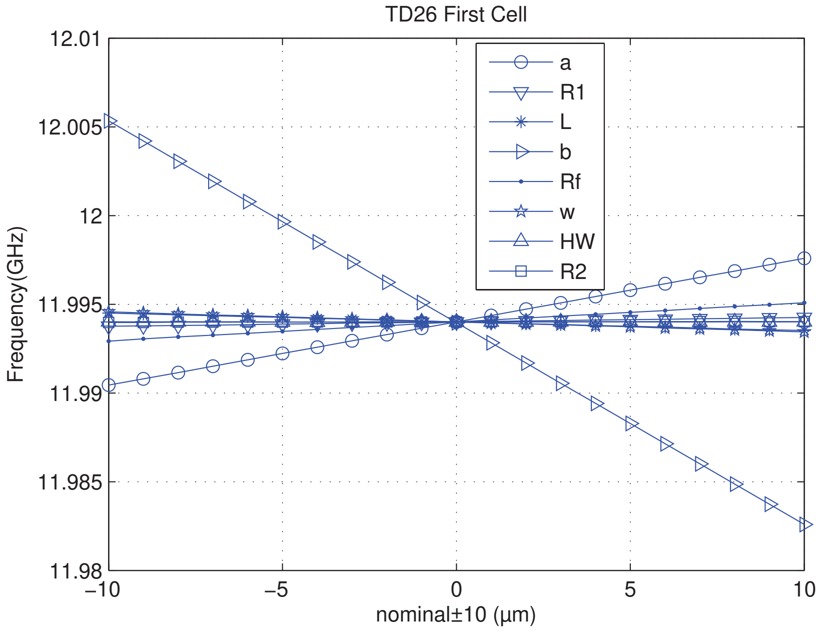

Figure 2.17. Sensitivity comparison of TD26 First Cell geometrical parameters

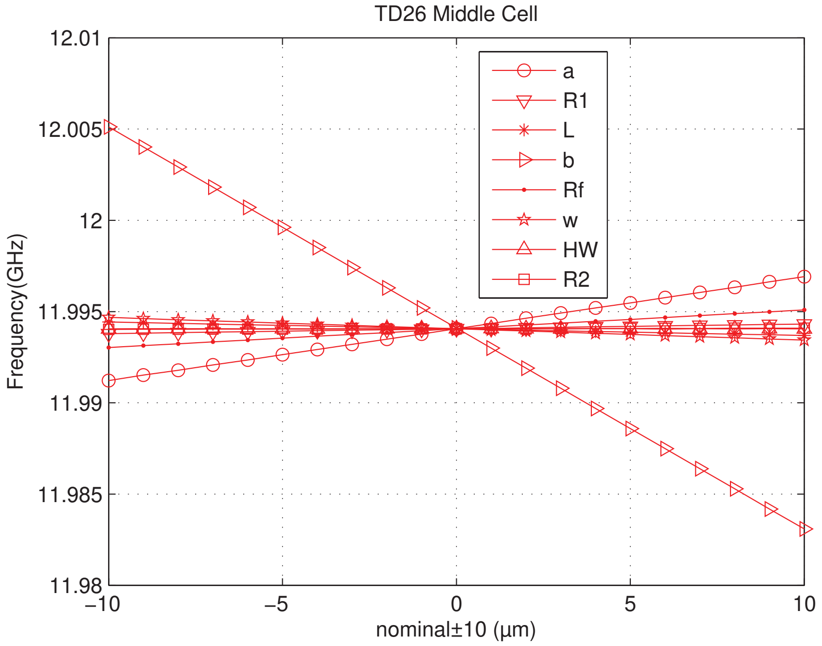

Figure 2.18. Sensitivity comparison of TD26 Middle Cell geometrical parameters

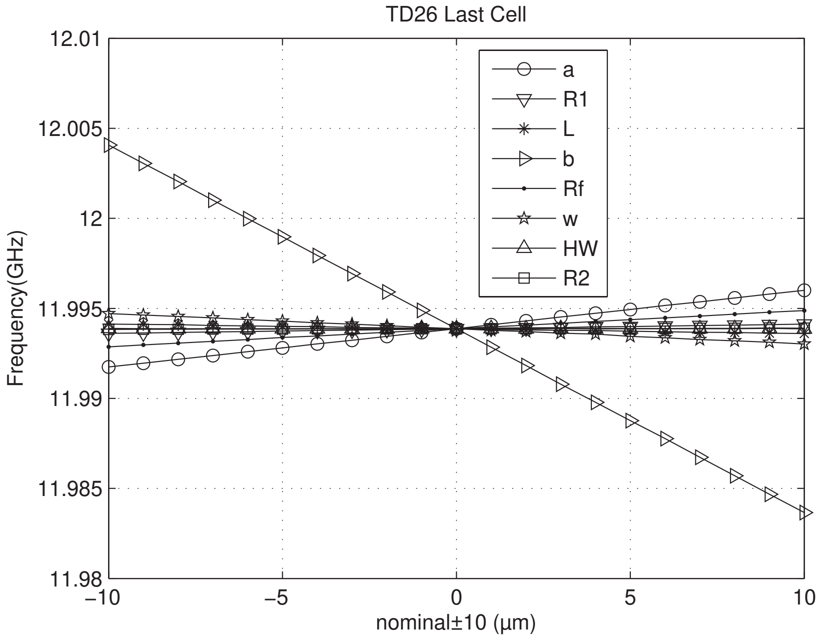

Figure 2.19. Sensitivity comparison of TD26 Last Cell geometrical parameters

Table 2.6. Nominal values of TD26 First, Middle and Last cells

Parameter	First Cell(mm)	Middle Cell(mm)	Last Cell(mm)
a	3.15	2.75	2.35
R1	0.7	0.7	0.7
L	8.3316	8.3316	8.3316
b	8.7038	8.5249	8.2774
Rf	1	1	1
w	10.1	10.1	10.1
HW	30	30	30
R2	2	2	2

Table 2.7. Δf for 1 μm change in parameters of TD26 cells

Parameter	First Cell(MHz)	Middle Cell(MHz)	Last Cell(MHz)
a	0.357	0.285	0.213
b	1.138	1.102	1.020
L	0.049	0.037	0.026
HW	0.0008	0.012	0.0014
w	0.056	0.062	0.084
R1	0.025	0.026	0.025
R2	0.003	0.003	0.004
Rf	0.108	0.103	0.101

The same decreasing behaviour of the frequency deviations for 1 μm change on dimensions is still valid for TD26 structure because of tapered feature.

2.11.4. Frequency Deviation Results From Simulations

According to sensitivity analysis results of both T24 and TD26 cells, the most important geometrical parameter related to frequency deviation is 'b' that is an inner radius of both cells as presented in previous sections.

The frequency sensitivity importance of the geometrical parameters for T24;
b>a>d>h>rr
The frequency sensitivity importance of the geometrical parameters for TD26;
b>a>Rf>w>L>R1>R2>HW

Given these results, we decided to concentrate our attention on the geometrical correlation between the inner radius imperfections and the single cell resonant frequency. Frequency variation due to a 1 μm change in 'b' for every cell in T24 and TD26 were simulated and are shown in Figure 2.20 and 2.21 respectively.

In order to investigate the geometrical correlation, inner radius imperfections were taken into account. 1 μm change in 'b' of T24 and TD26 causes frequency deviations in the cells as given in Table 2.8.

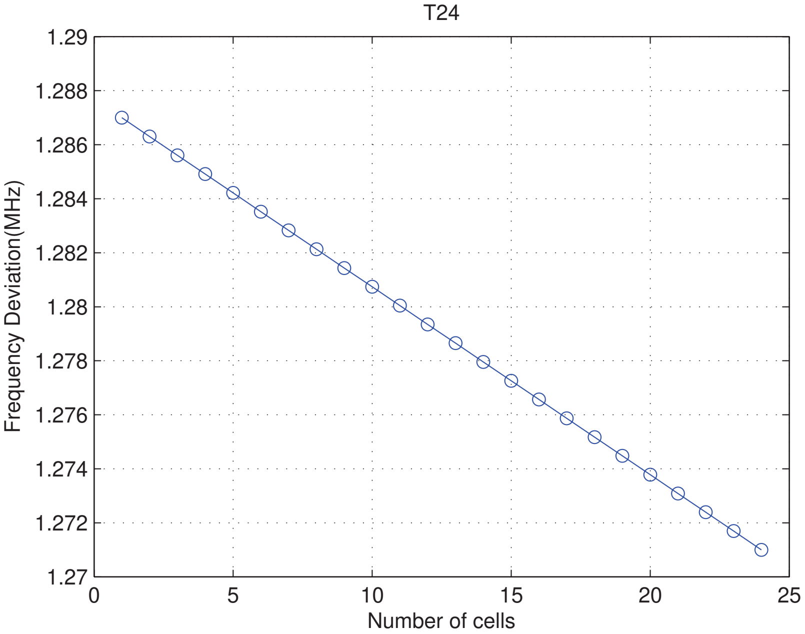

Figure 2.20. Linear interpolation of frequency deviations for T24 cells

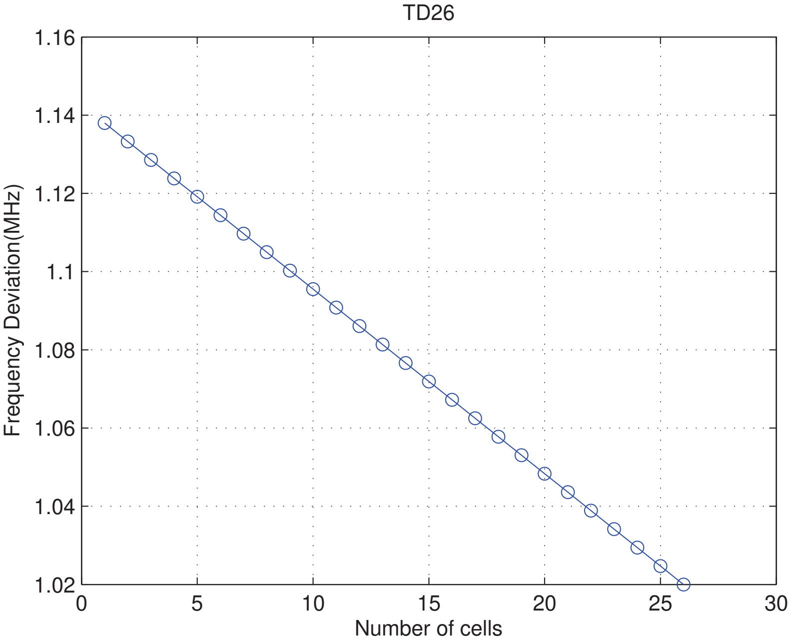

Figure 2.21. Linear interpolation of frequency deviations for TD26 cells

Table 2.8.: Δf of each cell according to 1 μm change in 'b'

	T24	**TD26**
Cell No.	**Δf(MHz)**	**Δf(MHz)**
1	1.2870	1.1380
2	1.2863	1.1333
3	1.2856	1.1286
4	1.2849	1.1238
5	1.2842	1.1191
6	1.2835	1.1144
7	1.2828	1.1097
8	1.2821	1.1050
9	1.2814	1.1002
10	1.2807	1.0955
11	1.2800	1.0908
12	1.2793	1.0861
13	1.2787	1.0814
14	1.2780	1.0766
15	1.2773	1.0719
16	1.2766	1.0672
17	1.2759	1.0625
18	1.2752	1.0578
19	1.2745	1.0530
20	1.2738	1.0483
21	1.2731	1.0436
22	1.2724	1.0389
23	1.2717	1.0342
24	1.2710	1.0294
25		1.0247
26		1.0200

CHAPTER 3

METHODOLOGY

We use the inner radius of each cell as we saw in the last chapter that is the most sensitive parameter to which the frequency. We measured by microscope. The frequency deviations were calculated from the bead-pull measurements. In this chapter, we describe the methodology to investigate the correlation between geometrical and RF characteristics of cells.

3.1. Sensitivity of Cell Frequency to Geometrical Parameters

In the design of T24 and TD26 structures both of them have the operating mode TM_{010} with $2\pi/3$ phase advance. The operating frequency of both structures was determined by the dispersion relation of the disc loaded structures (3.1) by the formula 3.1 given below where b, a, L and α represents the inner radius, iris aperture,distance between the discs and attenuation per unit length respectively [6].

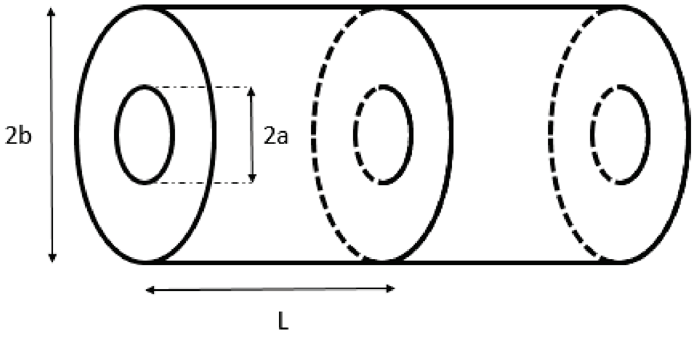

Figure 3.1. Disc Loaded Structure

$$\omega = \frac{2.405c}{b}\sqrt{1+\kappa(1-\cos(k_z L)e^{-\alpha h})} \tag{3.1}$$

$$\kappa = \frac{4a^3}{3\pi J_1^2(2.405)b^2 L} \ll 1 \tag{3.2}$$

$$\alpha = \frac{2.405}{a} \tag{3.3}$$

Phase velocity (υ_{ph}) and group velocity (υ_g) can be calculated from the formulas 3.4 and 3.5(where $\varphi = k_z L$ and c is the speed of light)[6];

$$\upsilon_{ph} = \frac{\omega}{k_z} = \frac{2.405cL}{b\varphi}\sqrt{1+\kappa(1-cos(k_z L))e^{-\alpha h}} \tag{3.4}$$

$$\upsilon_g = \frac{\mathrm{d}\omega}{\mathrm{d}k_z} = \frac{(2.405)^2 c\lambda a^3}{3\pi^2 J_1^2(2.405)b^4} e^{-\alpha h} sin(\varphi) \tag{3.5}$$

As seen from the formulas, the most sensitive parameter for the frequency is the inner radius named as ’b’ for both of the RF designs of T24 and TD26.

For damped disks, the radius is given by the distance of the centre of the iris to the tip of the four noses of the waveguide. For each disc, the b parameter is slightly different.

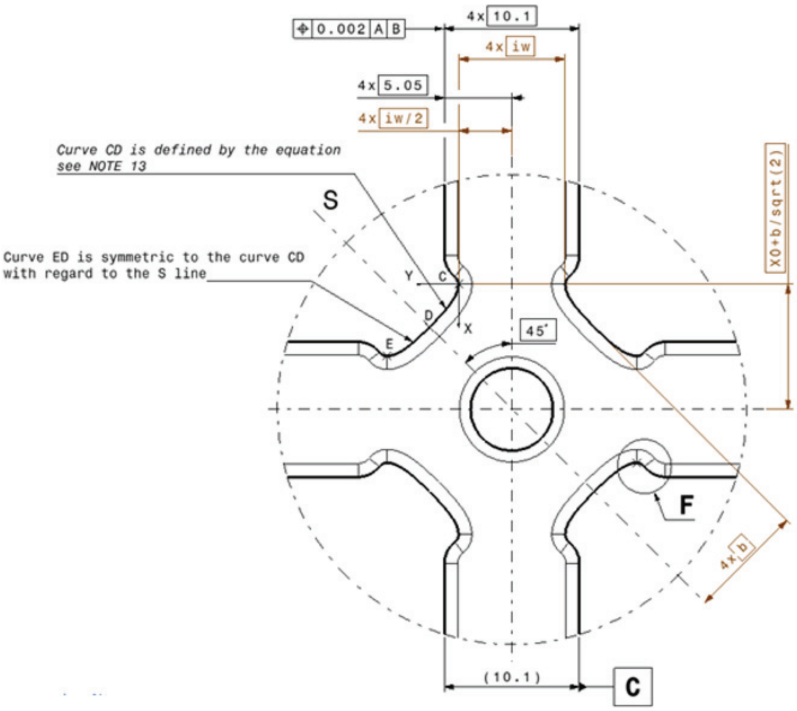

Figure 3.2. Technical Drawing of TD26 disc [25]

3.2. Measurements of The ’b’ Parameter of T24 and TD26 Cells by Microscope

All discs were measured in a Coordinate Measuring Machine (CMM) with a contact probe. The form of the 4 noses was controlled, nevertheless, the dimensions of the b parameter were not taken. The sensitivity of the b parameter was identified when the measurements were completed by the manufacturer. Since every measurement increase the risk of scratching the discs, it was decided to perform the measurement of the b parameter with an optic (non-contact) microscope.

In this work, the measurements for inner radius that belong to T24 N4, N5 and TD26 N1, N2 disc stacks were done and used for investigating the geometrical correlation. The inner radius measurements were done by an optical microscope in a clean room with the algorithm explained in the next section.

The discs were kept in a clean room that has a controlled temperature of 20 ± 1°C to avoid the expansion of the discs according to temperature change and other kind of deflections.

The measurements were done with the Vision Engineering Mono Optical Microscope with an optic zoom x100. The microscope has a measurement accuracy of U952D=4+(5.5L/100)μm.

Figure 3.3. Vision Engineering Hawk Mono Optical Microscope [27]

3.2.1. Measurement Procedure

The inner radius measurements of T24 and TD26 disc stacks were done according to measurement procedure given below. The evaluation of the circle is done by a least squares circle-fitting method. Moreover, repeatability (same operator, same disc) and reproducibility (different operator, same disc) were considered. For both repeatability and reproducibility considerations, we observed deviations of 1 μm.

According to least squares circle-fitting method;

$$(x_i, y_i), i = 0, 1, 2, 3, ..., N \tag{3.6}$$

obtain a circle by the formula;

$$(x - x_0)^2 + (y - y_0)^2 = R^2 \tag{3.7}$$

with a minimum square error.

The fundamental attitude of this method is obtaining a circle that has a mean distance from the given dataset is minimum. The measurement procedure follows the steps given below. The method is divided in alignment and measurement.

For the alignment;

1. Alignment of the disc with the Y axis of the device manually
2. Focus the top plane of the disc
3. Marking 4 points to obtain external diameter of the disc and obtaining circle (least square estimation)
4. Setting the reference (x, y)=(0, 0) at the centre of the iris

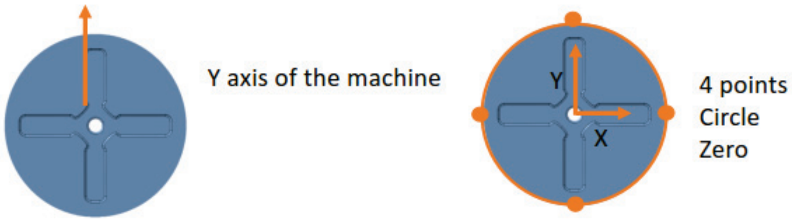

Figure 3.4. Y-axis of the machine (left) and reference obtained disc with 4 points (right)

For the measurement;

5. Mark point 1, then move and mark point 2 with only changing X-axis (Y-axis is fixed), do the same procedure for point 3 and point 4 with only changing one axis
6. Obtain the circle 1 (least square estimation)
7. Repeat the same procedure in step 4 with starting X-axis fixed in point 1
8. Obtain the circle 2 (least square estimation)

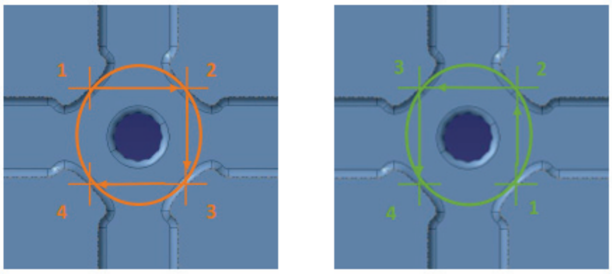

Figure 3.5. Marking direction for circle 1 (left) and for circle 2 (right)

9. Compare the calculated radius values and, if the values agree within 1 μm finish the measurement, otherwise repeat the procedure

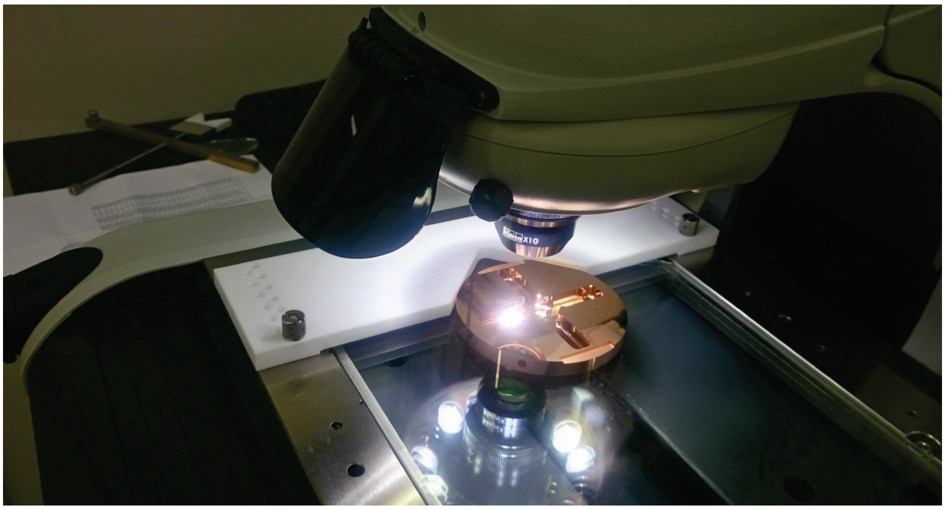

Figure 3.6. TD26 disc under dimension measurement by microscope

3.2.2. Measurement Results of T24 and TD26

The inner radius ’b’ measurement and deviation results for T24 N4, N5 disc stacks and TD26 N1, N2, N3 and N4 disc stacks obtained as given in Table 3.1, Table 3.2 and Table 3.3 respectively.

Table 3.1.: T24 N4 and N5 disc stacks ’b’ and ’Δb’ values

	T24 N4			**T24 N5**		
Disc No.	**Nominal (mm)**	**Measured (mm)**	**Deviation (μm)**	**Nominal (mm)**	**Measured (mm)**	**Deviation (μm)**
1	9.968	9.9672	0.8	9.967	9.9672	-0.2
2	9.956	9.9545	1.5	9.955	9.9545	0.5
3	9.944	9.942	2	9.944	9.942	2
4	9.929	9.9297	-0.7	9.932	9.9297	2.3
5	9.918	9.9177	0.3	9.919	9.9177	1.3
6	9.905	9.906	-1	9.907	9.906	1
7	9.896	9.8944	1.6	9.895	9.8944	0.6
8	9.883	9.8831	-0.1	9.885	9.8831	1.9
9	9.873	9.8721	0.9	9.874	9.8721	1.9
10	9.862	9.8613	0.7	9.863	9.8613	1.7
11	9.851	9.8507	0.3	9.853	9.8507	2.3
12	9.84	9.8404	-0.4	9.842	9.8404	1.6
13	9.831	9.8302	0.8	9.83	9.8302	-0.2
14	9.822	9.8204	1.6	9.823	9.8204	2.6
15	9.811	9.8108	0.2	9.811	9.8108	0.2
16	9.802	9.8014	0.6	9.803	9.8014	1.6
17	9.794	9.7922	1.8	9.794	9.7922	1.8
18	9.784	9.7833	0.7	9.784	9.7833	0.7
19	9.776	9.7746	1.4	9.776	9.7746	1.4
20	9.767	9.7662	0.8	9.767	9.7662	0.8
21	9.759	9.758	1	9.759	9.758	1
22	9.75	9.75	0	9.752	9.75	2
23	9.744	9.7423	1.7	9.745	9.7423	2.7

(Continued on next page)

Table 3.1 (cont.)

	T24 N4			**T24 N5**		
Disc No.	**Nominal (mm)**	**Measured (mm)**	**Deviation (μm)**	**Nominal (mm)**	**Measured (mm)**	**Deviation (μm)**
24	9.736	9.7348	1.2	9.736	9.7348	1.2

Table 3.2.: TD26 N1 and N2 disc stacks ’b’ and ’Δb’ values

		TD26 N1		**TD26 N2**	
Disc No.	**Nominal (mm)**	**Measured (mm)**	**Deviation (μm)**	**Measured (mm)**	**Deviation (μm)**
1	8,6987	8,696	2.7	8,695	3.7
2	8,685	8,684	1	8,683	2
3	8,6724	8,672	0.4	8,672	0.4
4	8,66	8,66	0	8,658	2
5	8,6468	8,647	-0.2	8,646	0.8
6	8,6337	8,632	1.7	8,631	2.7
7	8,6202	8,619	1.2	8,619	1.2
8	8,6064	8,605	1.4	8,605	1.4
9	8,5921	8,591	1.1	8,591	1.1
10	8,5778	8,576	1.8	8,577	0.8
11	8,5629	8,563	0.1	8,562	0.9
12	8,5478	8,546	1.8	8,546	1.8
13	8,5324	8,531	1.4	8,531	1.4
14	8,5166	8,516	0.6	8,515	1.6
15	8,5003	8,499	1.3	8,499	1.3
16	8,4841	8,482	2.1	8,482	2.1
17	8,4669	8,465	1.9	8,466	0.9
18	8,4493	8,448	1.3	8,448	1.3
19	8,4313	8,431	0.3	8,43	1.3
20	8,4124	8,411	1.4	8,41	2.4
21	8,3936	8,391	2.6	8,392	1.6

(Continued on next page)

Table 3.2 (cont.)

		TD26 N1		TD26 N2	
Disc No.	**Nominal (mm)**	**Measured (mm)**	**Deviation (μm)**	**Measured (mm)**	**Deviation (μm)**
22	8,3738	8,372	1.8	8,373	0.8
23	8,3533	8,351	2.3	8,351	2.3
24	8,3325	8,331	1.5	8,331	1.5
25	8,3108	8,309	1.8	8,309	1.8
26	8,2878	8,286	1.8	8,286	1.8

Table 3.3.: TD26 N3 and N4 disc stacks ’b’ and ’Δb’ values

		TD26 N3		TD26 N4	
Disc No.	**Nominal (mm)**	**Measured (mm)**	**Deviation (μm)**	**Measured (mm)**	**Deviation (μm)**
1	8.6987	8.695	3.7	8.694	4.7
2	8.685	8.682	3	8.683	2
3	8.6724	8.673	-0.6	8.672	0.4
4	8.66	8.658	2	8.658	2
5	8.6468	8.645	1.8	8.647	-0.2
6	8.6337	8.631	2.7	8.634	-0.3
7	8.6202	8.618	2.2	8.619	1.2
8	8.6064	8.607	-0.6	8.604	2.4
9	8.5921	8.59	2.1	8.591	1.1
10	8.5778	8.576	1.8	8.578	-0.2
11	8.5629	8.561	1.9	8.561	1.9
12	8.5478	8.546	1.8	8.547	0.8
13	8.5324	8.533	-0.6	8.531	1.4
14	8.5166	8.515	1.6	8.517	-0.4
15	8.5003	8.497	3.3	8.5	0.3
16	8.4841	8.484	0.1	8.484	0.1
17	8.4669	8.465	1.9	8.464	2.9

(Continued on next page)

Table 3.3 (cont.)

		TD26 N3		TD26 N4	
Disc No.	**Nominal (mm)**	**Measured (mm)**	**Deviation (μm)**	**Measured (mm)**	**Deviation (μm)**
18	8.4493	8.449	0.3	8.449	0.3
19	8.4313	8.43	1.3	8.431	0.3
20	8.4124	8.413	-0.6	8.411	1.4
21	8.3936	8.392	1.6	8.392	1.6
22	8.3738	8.374	-0.2	8.372	1.8
23	8.3533	8.35	3.3	8.35	3.3
24	8.3325	8.33	2.5	8.33	2.5
25	8.3108	8.306	4.8	8.308	2.8
26	8.2878	8.284	3.8	8.284	3.8

3.3. Theory and Application of Bead-pull Measurement Method

In this section, we present the bead-pull method using non-resonant perturbation theory. We will also describe the setup at CERN and present the measurement results for structures before and after bonding.

3.3.1. Non-resonant Perturbation Theory

This theory is based on obtaining an approximate solution by adding a small deviation to the desired parameter. When a small object enters a volume contains electromagnetic field, it causes a change in energy stored and produces a frequency deviation. As illustrated in Figure 3.7, the volume properties changed after perturbation.

This theory can be applied any device that has the following properties;

- Includes an electromagnetic field inside.
- The power applied to the device should enter from only one port where the perturbation measurements were done.
- There should be a single mode TE, TM or TEM at the place where the reflection coefficient measurements were done.

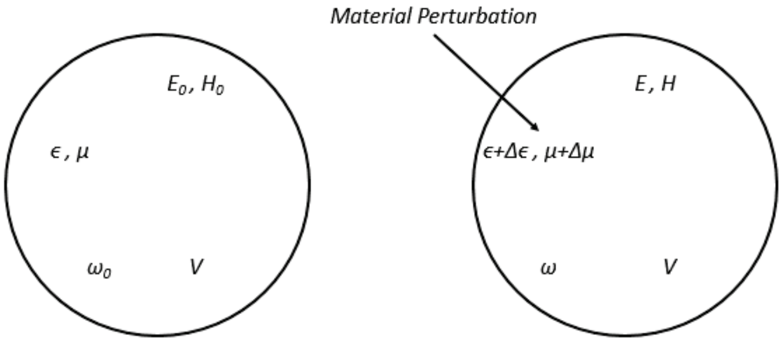

Figure 3.7. Volume before (left) and after (right) material perturbation

- The device walls should provide a good isolation between its inside and outside for electromagnetic waves at the working frequency.
- The device walls and inside should be assumed to have electrical parameters which are linear and isotropic [28].

3.3.2. Bead-pull Measurement Method

Bead-pull method is an RF measurement technique that is based on a non-resonant perturbation theory. It is developed for determining the electric and magnetic field profile inside the RF cavities and also frequency tuning of the structure after assembling process.

According to non-resonant perturbation theory when small object enters the volume contains electromagnetic field, it changes the energy stored and causes frequency change as given in previous section. The frequency change can be calculated approximately by the formula 3.8 given below where Δf is frequency change after perturbation, f_0 is operating frequency, Δf is volume after perturbation and V_0 is volume before perturbation, H and E represents magnetic and electric fields respectively [10].

$$\frac{\triangle f}{f_0} = \frac{\oint_{\triangle V}(\mu_0|H|^2 - \varepsilon_0|E|^2)dV}{\oint_{V_0}(\mu_0|H|^2 + \varepsilon_0|E|^2)dV} \tag{3.8}$$

Both dielectric or conducting bead can be used according to field to be measured. If metallic (conducting) bead is used both electric and magnetic fields can be measured. If dielectric bead is used only electric field can be measured inside the cavity.

The bead-pull measurement setup can be set both vertically or horizontally. As illustrated in the Figure 3.8, the setup includes step motors to move the bead inside the cavity, Vector Network Analyzer (VNA) to measure the cavity resonance and a computer to register and process the data from VNA by a novel software interface. For the bead-pull measurement, the algorithm given in Figure 3.9 was used.

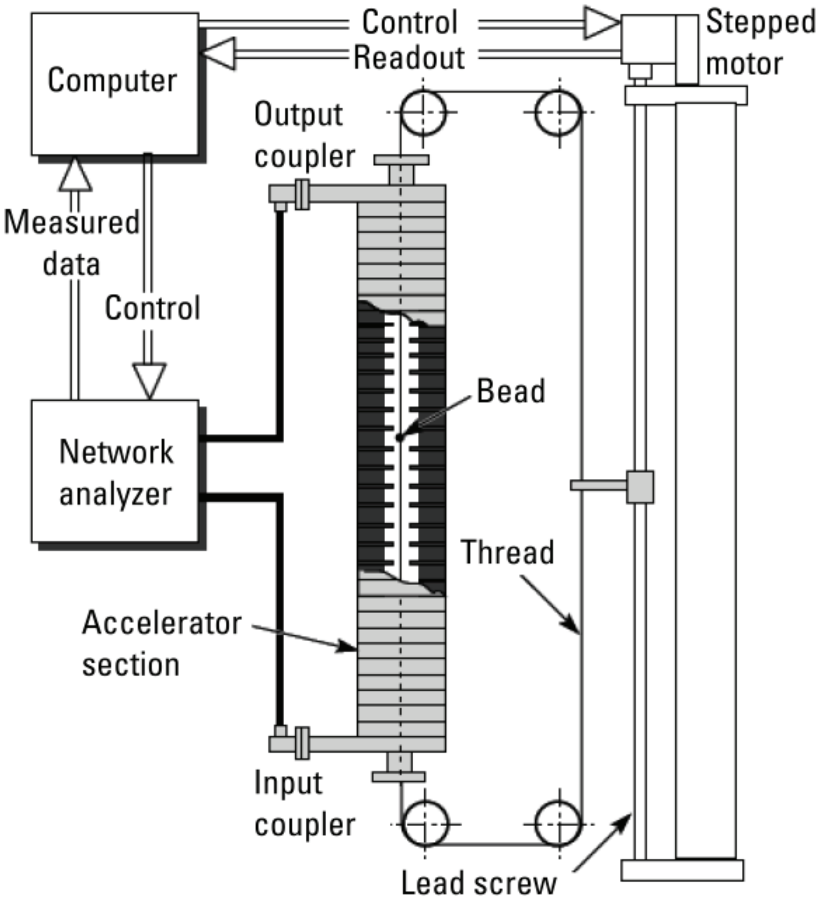

Figure 3.8. Schematic of bead-pull system [16]

While the bead-pull measurement process, the temperature of the structure and the insertion of wire inside the structure must be taken into account. A change of 1 °C in temperature produces a change of 200 kHz in the operating frequency, reverse of it also valid as mentioned in Chapter 1 (see Section 1.4.9). The wire that holds the bead causes approximately 0.5 MHz shift in frequency when it is inside the cavity. Due to usage of the open parts (beam pipes) of the structure for wire, it is not possible to apply N_2 inside the cavity. Then, lack of N_2 causes humidity. This decreases the precision of measurement according to incalculable air effects.

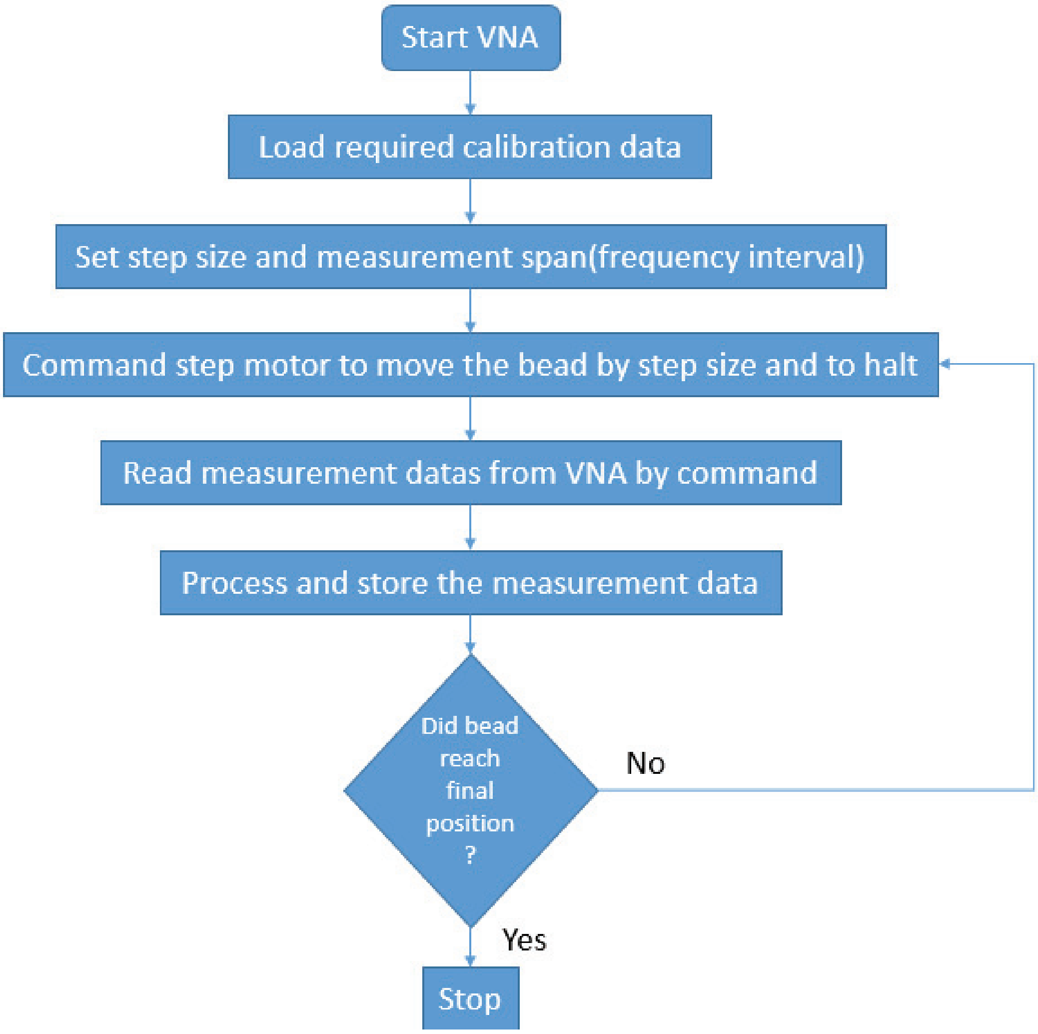

Figure 3.9. Algorithm for bead-pull measurement

3.3.3. Bead-pull Measurement Setups at CERN

There are two bead-pull setups at CERN as illustrated in Figure 3.10. One is fixed test bench that was set vertically. The other is movable test bench that designed and manufactured for only use in bead-pull measurement before bonding process of discs with a desired position horizontally or vertically. It has an adjustable input/output coupler parts and this feature gives flexibility to set better contact with VNA.

Both setups are placed in a clean room that has a stable temperature and includes 4-port Rochde&Schwarz ZVA 24 GHz Vector Network Analyzer for all the RF measurements and tuning process of accelerating structures.

Figure 3.10. Fixed Test Bench (left) and Movable Test Bench (right) [26]

3.3.4. Obtaining Individual Frequency Deviations of The Cells From Bead-pull Measurement Method

In order to investigate the geometrical correlation between the inner radius of the discs and frequency deviations, the individual frequency deviations of the accelerating cells must be obtained from the bead-pull measurement both before and after bonding process.

The measurement of the structures were done and analysed by a novel software that was coded by MATLAB [31] in order to bead-pull and tuning procedure of the prototype accelerating structures.

The calculation of the frequency deviations of cells based on the individual reflection coefficient of each cell where Γ is local S_{11} parameter of the cells, β is the coupling coefficients of the cells, and f_0 is the design frequency and Q_0 is an intrinsic Q-factor [32];

$$\Gamma = \frac{\beta - 1}{2} + j\frac{Q_0^{'}\triangle f_0}{f_0} \tag{3.9}$$

The local S_{11} parameters are obtained by the calculation of the backward (B_n) and forward waves (A_n) which passing through for each cell individually by tuning software and formulas where I_n is the superposition of backward and forward waves inside the cell.

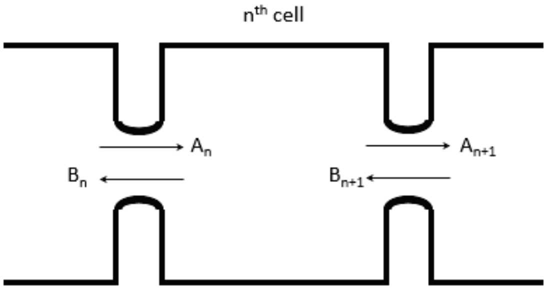

Figure 3.11. Forward and Backward waves passing through a cell

$$A_n = \frac{I_{n-1} - I_n e^{-j\varphi}}{2jsin(\varphi)} \tag{3.10}$$

$$B_n = \frac{I_{n-1} - I_n e^{j\varphi}}{-2jsin(\varphi)} \tag{3.11}$$

The formula for local S_{11} parameter of the cells except first and last cell is derived as;

$$S_{11}^{local|n} = \frac{B_n - B_{n+1}e^{-j\varphi}}{A_n}, (2 \leq n \leq N-1) \tag{3.12}$$

The output matching(last) cell is terminated with a matched load which damps reflection, so the local S_{11} formula of last cell is;

$$S_{11}^{local|N} = \frac{B_N}{A_N} \tag{3.13}$$

For the input matching(first) cell, formula of local S_{11} is expressed as;

$$S_{11}^{local|1} = \frac{[-j|\triangle S_{11}^{b.p.(1)}|/\triangle S_{11}^{b.p.(1)}]S_{11}A_1 - B_2 e^{-j\varphi}}{A_1} \tag{3.14}$$

where S_{11} is the reflection of whole structure and $\triangle S_{11}^{b.p.(1)}$ is the reflection caused by bead in the first cell with a φ_0 phase offset.

$$S_{11} = e^{-2j\varphi_0}\frac{B_1}{A_1} \tag{3.15}$$

$$\triangle S_{11}^{b.p.(1)} = e^{-2j\varphi_0}(-j|\triangle S_{11}^{b.p.(1)}|) \tag{3.16}$$

The frequency deviation of each cell is obtained by the formula 3.18 where $Q_0^{'}$, c, φ and υ_g represents an intrinsic Q-factor, speed of light, phase advance between the cells and group velocity respectively. Also f_0, f_{target} and f_{bp} represents the design frequency, target frequency in measurement conditions and frequency of bead-pull measurement respectively.

$$Q_0^{'} = \frac{c\varphi}{v_g} \tag{3.17}$$

$$\triangle f = \frac{Im(S_{11local})}{c\frac{\varphi}{v_g}} f_0 + (f_{target} - f_{bp}) \tag{3.18}$$

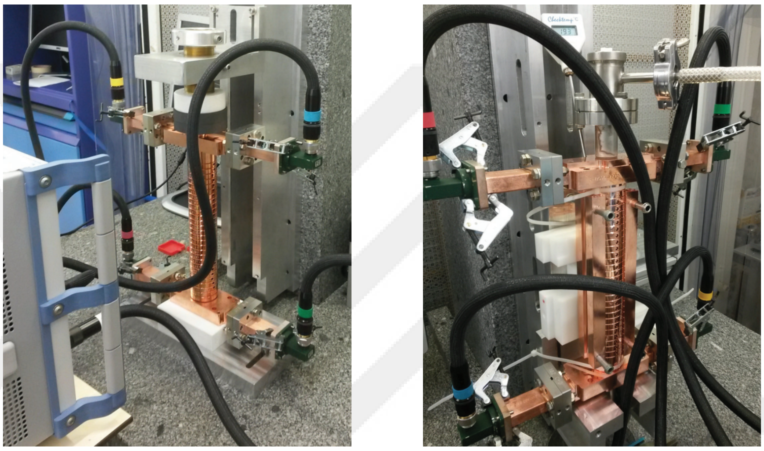

Figure 3.12. T24 Bead-pull Measurement Setups Before (left) and After (right) Bonding

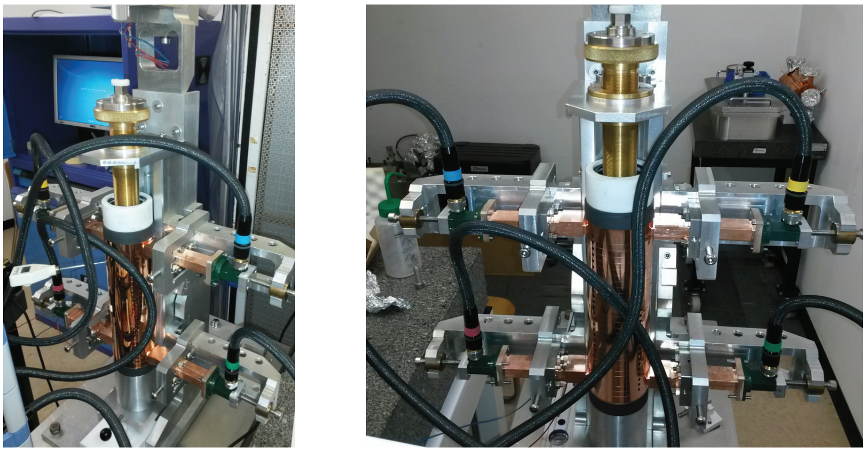

Figure 3.13. TD26 Bead-pull Measurement Setups Before (left) and After (right) Bonding

3.3.4.1. Individual Frequency Deviations of T24 Cells for N4 and N5 Disc Stacks

Four bead-pull measurements were done for T24 disc stack N4 and N5 before and after bonding process. The frequency deviations were obtained as illustrated in Table 3.4 given below.

Table 3.4.: Δf T24 N4 and N5 cells obtained from bead-pull before and after bonding

	T24 N4		**T24 N5**	
Cell No.	**Before Bonding Δf(MHz)**	**After Bonding Δf(MHz)**	**Before Bonding Δf(MHz)**	**After Bonding Δf(MHz)**
1	2.473	1.5892	2.5126	0.47
2	1.34	0.0316	2.1437	1.1553
3	2.369	1.4668	2.64	1.5125
4	7.209	1.1259	3.1139	1.2365
5	2.2	1.0387	2.688	0.1966
6	2.29	1.3631	3.4605	2.2553
7	3.667	0.5932	4.1041	0.8005
8	1.551	0.0592	2.4334	0.813
9	2.126	0.7023	2.7844	1.2608
10	3.149	0.8676	3.2557	1.0387
11	2.46	0.5269	2.5775	0.6148
12	1.292	0.7684	3.2503	1.1031
13	3.247	0.8612	2.9122	0.1924
14	2.705	0.6112	3.5232	1.2128
15	1.682	0.9778	4.0731	1.5488
16	2.801	0.4669	5.5971	0.7365
17	2.466	0.4544	4.1852	-0.0486
18	1.229	-0.0723	2.6562	1.0319
19	2.908	0.8727	2.5472	0.318
20	1.988	-0.4205	3.1595	0.1757
21	1.322	1.1651	4.6535	-0.2031

(Continued on next page)

Table 3.4 (cont.)

	T24 N4		**T24 N5**	
Cell No.	**Before Bonding Δf(MHz)**	**After Bonding Δf(MHz)**	**Before Bonding Δf(MHz)**	**After Bonding Δf(MHz)**
22	2.422	0.2834	2.9707	1.8164
23	2.454	0.2217	2.4218	0.5701
24	7.882	6.2452	8.9123	6.7753

3.3.4.2. Individual Frequency Deviations of TD26 Cells for N1, N2, N3 and N4 Disc Stacks

The same procedure for T24 applied to the TD26 disc stacks, bead-pull measurements were done for TD26 disc stack N1, N2, N3 and N4 before bonding process. However, for TD26 N1 structure, an assembling error occurred during the bonding process. Thus, bead-pull measurement after bonding are only available for N2 structure. The frequency deviations were obtained for N1, N2, N3 and N4 disc stacks as illustrated in Table 3.5 and 3.6 given below.

Table 3.5.: Δf of TD26 N1 and N2 cells obtained from bead-pull before and after bonding

	TD26 N1	**TD26 N2**	
Cell No.	**Before Bonding Δf(MHz)**	**Before Bonding Δf(MHz)**	**After Bonding Δf(MHz)**
1	-2.0593	-1.7488	-3.9791
2	1.3685	1.1682	-0.3147
3	0.6082	0.8328	-1.1392
4	1.3576	0.8491	-2.1477
5	1.0748	1.8947	1.0217
6	1.0764	0.8499	-0.6149
7	1.635	1.9402	-0.5201
8	1.054	0.8688	-0.827
9	1.2432	0.97	0.6429

(Continued on next page)

Table 3.5 (cont.)

	TD26 N1	**TD26 N2**	
Cell No.	**Before Bonding** Δf**(MHz)**	**Before Bonding** Δf**(MHz)**	**After Bonding** Δf**(MHz)**
10	1.7022	1.8144	-0.0826
11	1.8377	1.5517	0.466
12	1.3387	1.3712	0.9348
13	1.3045	1.1016	0.2765
14	1.3822	1.025	1.2478
15	0.9196	0.6693	1.1703
16	1.8055	1.5369	-0.4541
17	1.3722	0.4051	2.4566
18	0.9458	0.7525	0.5545
19	2.3531	2.1222	1.2359
20	0.4549	-0.4929	1.5397
21	1.4268	1.3024	1.8909
22	1.6242	1.5882	2.1232
23	1.5622	1.0588	2.4186
24	0.9828	1.6585	2.5386
25	2.7316	2.0203	2.1815
26	2.6986	1.7035	1.6512

Table 3.6.: Δf of TD26 N3 and N4 cells obtained from bead-pull before bonding

	TD26 N3	**TD26 N4**
Cell No.	**Before Bonding** Δf**(MHz)**	**Before Bonding** Δf**(MHz)**
1	-2.1372	-2.6641
2	0.4162	0.2289
3	0.0569	1.0477
4	0.8864	1.469
5	1.2873	1.7973

(Continued on next page)

Table 3.6 (cont.)

	TD26 N3	**TD26 N4**
Cell No.	**Before Bonding** Δf**(MHz)**	**Before Bonding** Δf**(MHz)**
6	0.426	0.6349
7	1.965	2.2077
8	0.731	0.7512
9	-0.2839	-0.1628
10	1.5091	1.5405
11	2.0503	0.7598
12	0.6645	0.1088
13	0.7758	1.5464
14	1.1329	0.7851
15	-0.538	0.0423
16	0.6403	0.6829
17	0.8382	0.7594
18	0.4715	1.4306
19	1.2614	0.4259
20	1.2775	0.7575
21	1.0742	1.7103
22	0.8949	1.5133
23	0.8232	-0.3403
24	1.8034	1.3771
25	1.5103	0.6479
26	1.2948	1.3284

CHAPTER 4

RESULTS

In this chapter, the correlation between inner radius imperfections and individual cell frequency changes for before and after bonding process are presented.

4.1. Introduction to Correlation function

Correlation is a data analysis function that gives the strength of the linear relationship between two different datasets. Correlation strength can be identified by a correlation coefficient, *r* that has the properties given below [34];

- Computed value of *r* is always in the range of -1 and +1 ($-1 < r < +1$).
- The magnitude and sign of the correlation coefficient represents the strength and magnitude of the relation.

  $-1.0 < r < -0.5$ negative strong correlation.
  $-0.5 < r < -0.3$ negative moderate correlation.
  $-0.3 < r < -0.1$ negative weak correlation.
  $+0.5 < r < +1.0$ positive strong correlation.
  $+0.3 < r < +0.5$ positive moderate correlation.
  $+0.1 < r < +0.3$ positive weak correlation.
  $-0.1 < r < +0.1$ none or very weak correlation.

The correlation coefficient is calculated by the following formula where (x, y) represents two different datasets and S$_{xx}$, S$_{yy}$ and S$_{xy}$ are the squared sums of deviations of x, y and their cross products [33].

$$r = \frac{S_{xy}}{\sqrt{S_{xx}}\sqrt{S_{yy}}} \tag{4.1}$$

$$S_{xy} = \sum (x - \overline{x})(y - \overline{y}) \tag{4.2}$$

$$S_{xx} = \sum (x - \overline{x})^2 \tag{4.3}$$

$$S_{yy} = \sum (y - \overline{y})^2 \tag{4.4}$$

4.2. Correlation Results for ’b’ Parameter and Frequency Change of T24 and TD26 Disc Stacks

In this section, the correlation graphs obtained for T24 and TD26 disc stacks are presented. The correlations between the inner radius imperfections and frequency deviations of the individual cells were obtained for T24 N4, N5 and TD26 N1, N2, N3, N4 disc stacks before bonding. However, as mentioned previous section, the bead-pull measurement of TD26 N1 disc stack after bonding is missing.

Due to the geometrical parameter sensitivity to frequency change simulation results of accelerating structure cells, the most sensitive parameter is determined as inner radius ’b’ (See 2.11) and it is inversely proportional to the frequency. So, we expect negative correlation between frequency change and inner radius deviation for both of the structures. According to correlation coefficients of T24 N4 and N5 disc stacks, there is no correlation between frequency deviations and inner radius imperfection as shown in Figures 4.1.and 4.2

According to correlation coefficients of TD26 disc stacks; N1 shows weak correlation, N2 shows negative strong correlation, N3 shows no correlation and N4 shows negative moderate correlation as shown in Figures 4.3, 4.4, 4.5 and 4.6 respectively. The correlation coefficients are not stable for all the disc stacks but all has a negative correlation as we expect due to the simulation results.

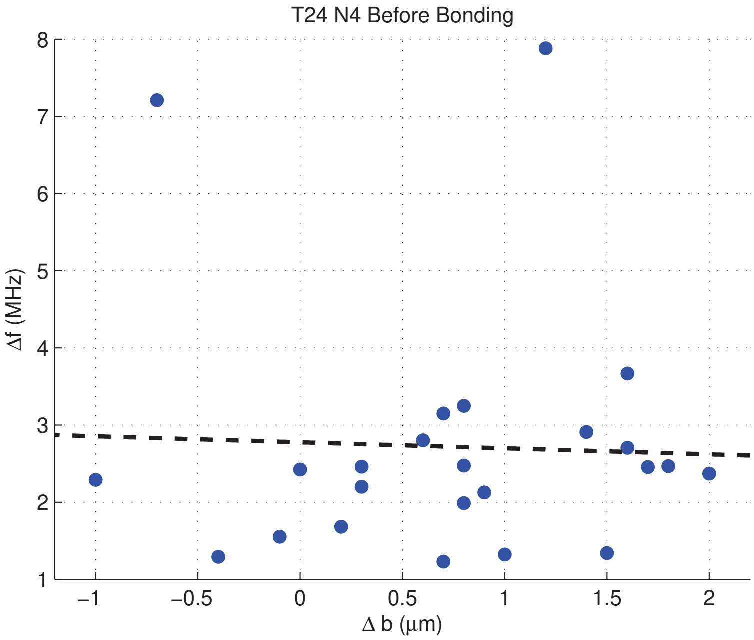

Figure 4.1. Scatterplot for T24 N4 Before Bonding, r = -0.038

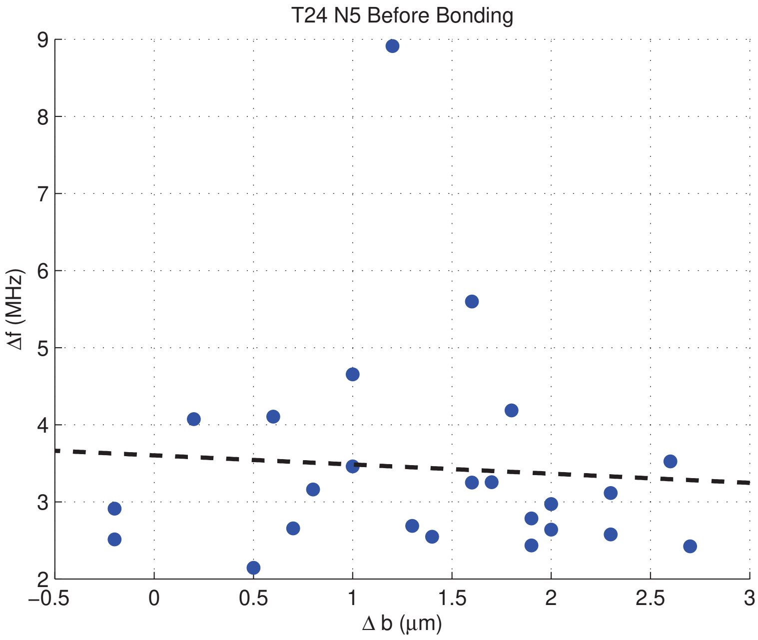

Figure 4.2. Scatterplot for T24 N5 Before Bonding, r = -0.069

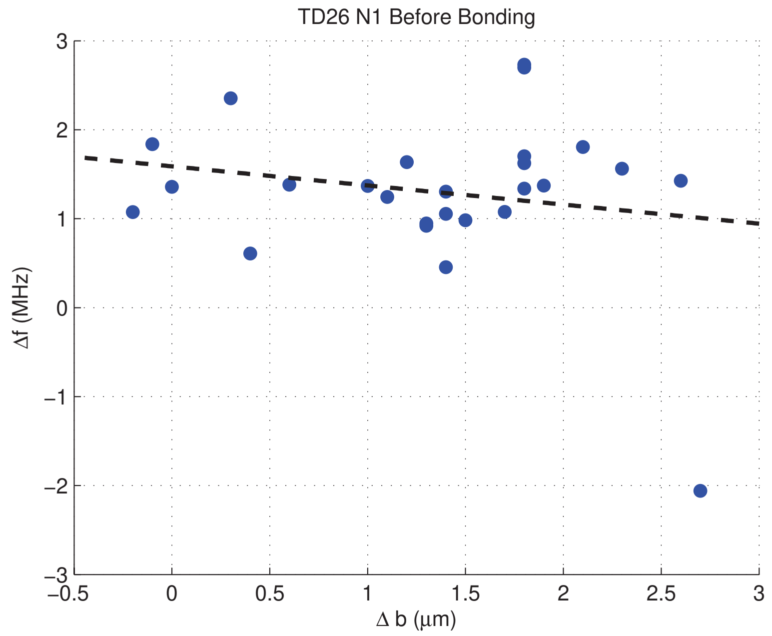

Figure 4.3. Scatterplot for TD26 N1 Before Bonding, r = -0.193

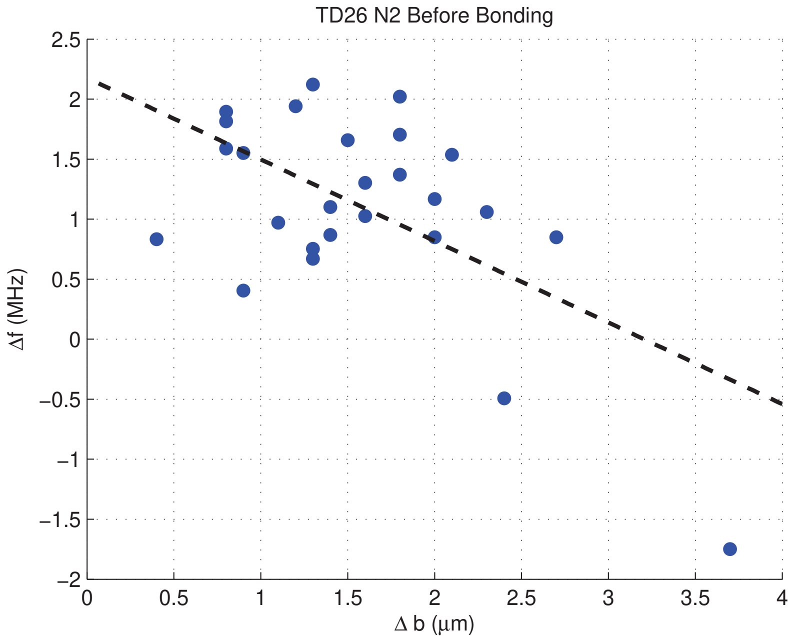

Figure 4.4. Scatterplot for TD26 N2 Before Bonding, r = -0.59

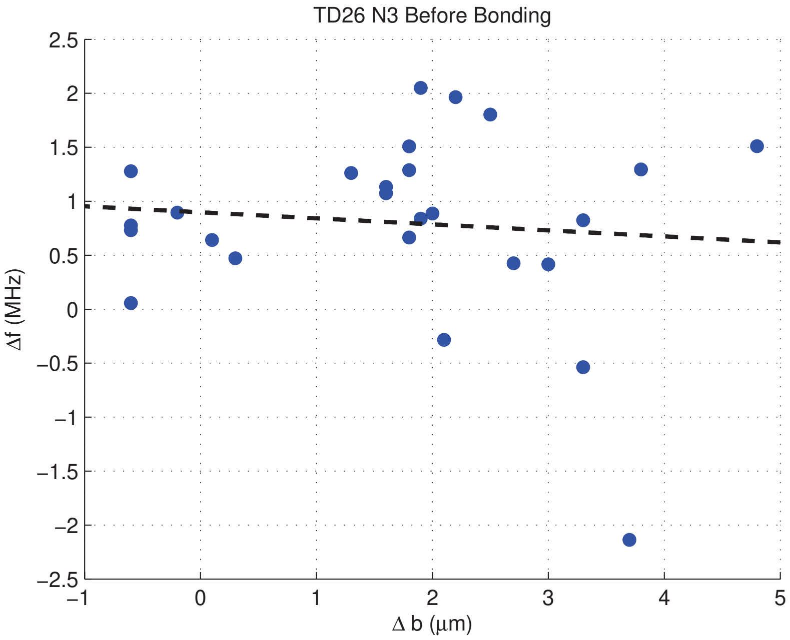

Figure 4.5. Scatterplot for TD26 N3 Before Bonding, r = -0.09

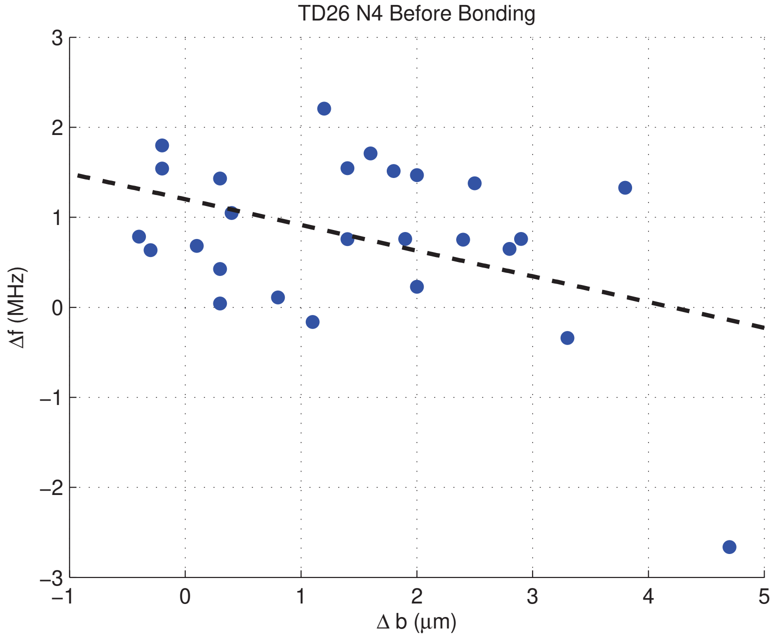

Figure 4.6. Scatterplot for TD26 N4 Before Bonding, r = -0.4

4.3. Frequency Change and Correlation Results for T24 N4, N5 and TD26 N2 Before and After Bonding

As seen from the Figures 4.7 and 4.8 for T24 N4 and N5, RF contact is better, frequency deviations are getting smaller after bonding process and the correlation coefficients between the frequency deviations before and after bonding process(Figure 4.9 and 4.10) have positive strong correlation which means bonding process did not deform the cells.

For TD26 N2 structure, frequency deviations before and after bonding process was obtained as illustrated in Figure 4.11 and there is a positive moderate correlation between them as shown in Figure 4.12.

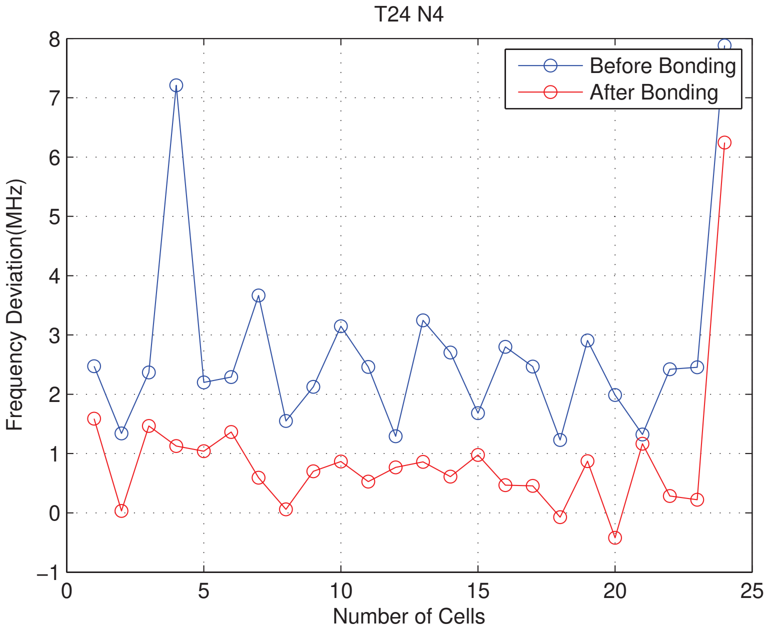

Figure 4.7. Frequency changes of T24 N4 structure before and after bonding

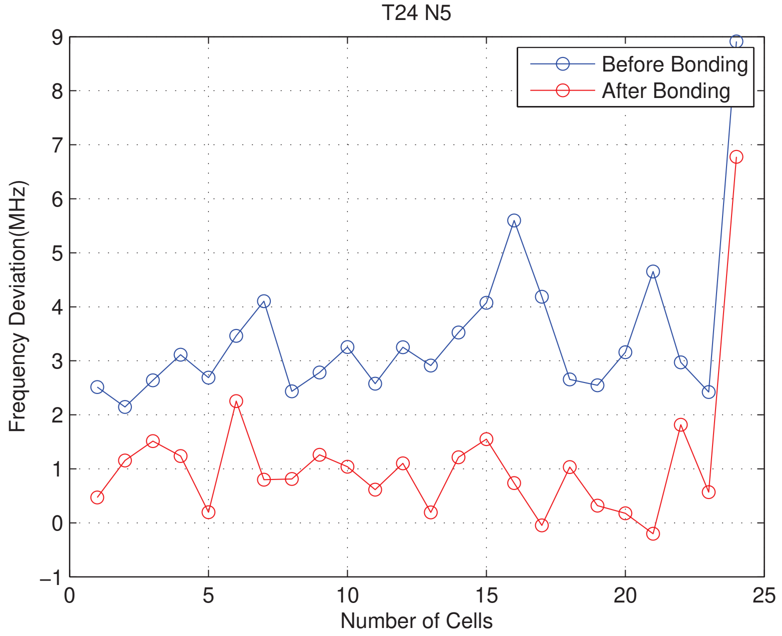

Figure 4.8. Frequency changes of T24 N5 structure before and after bonding

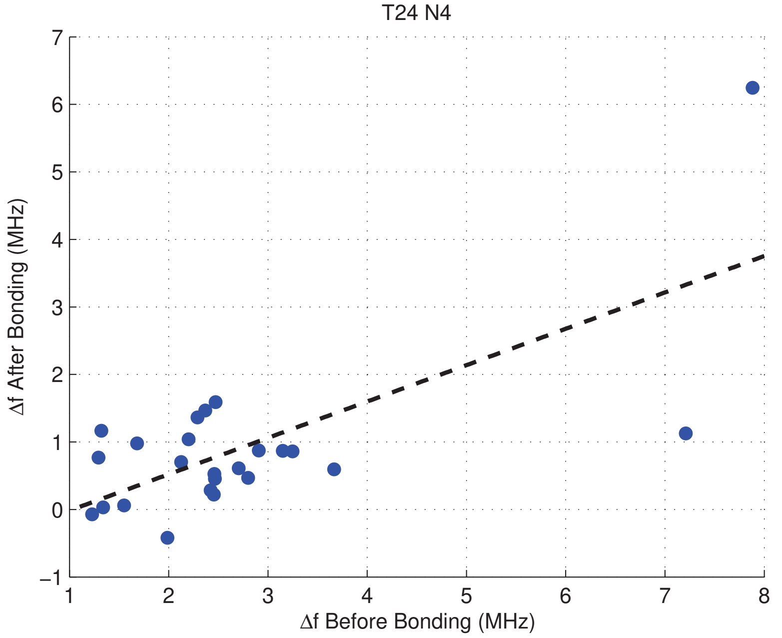

Figure 4.9. Linear correlation between the frequency deviations for T24 N4 before and after bonding process, $r = +0.703$

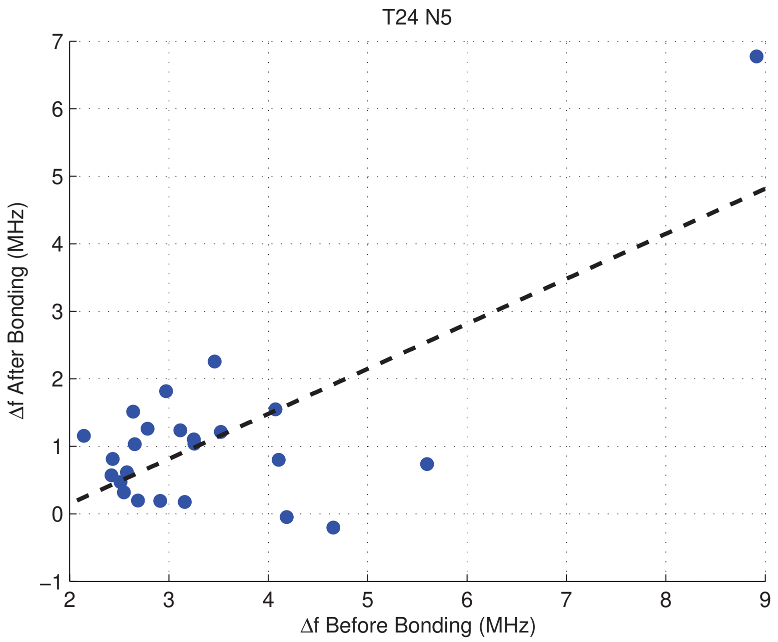

Figure 4.10. Linear correlation between the frequency deviations for T24 N5 before and after bonding process, $r = +0.704$

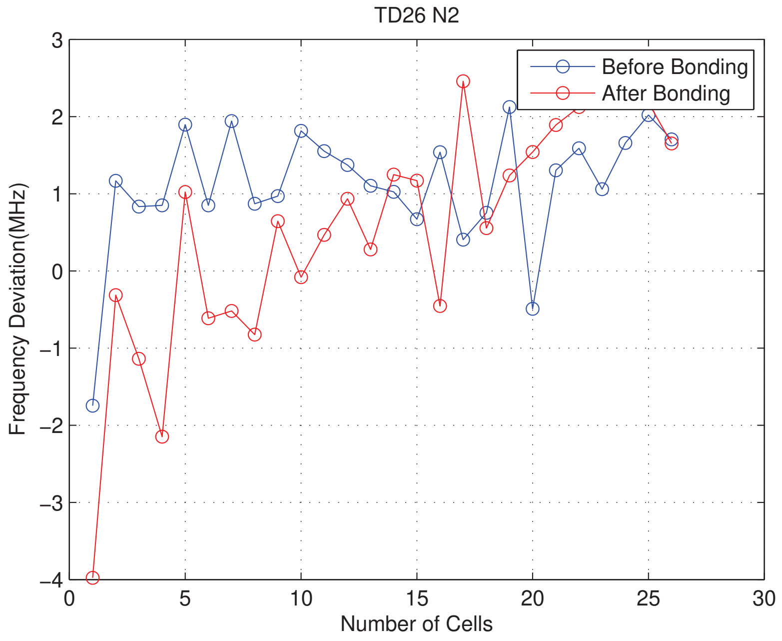

Figure 4.11. Frequency changes of TD26 N2 structure before and after bonding

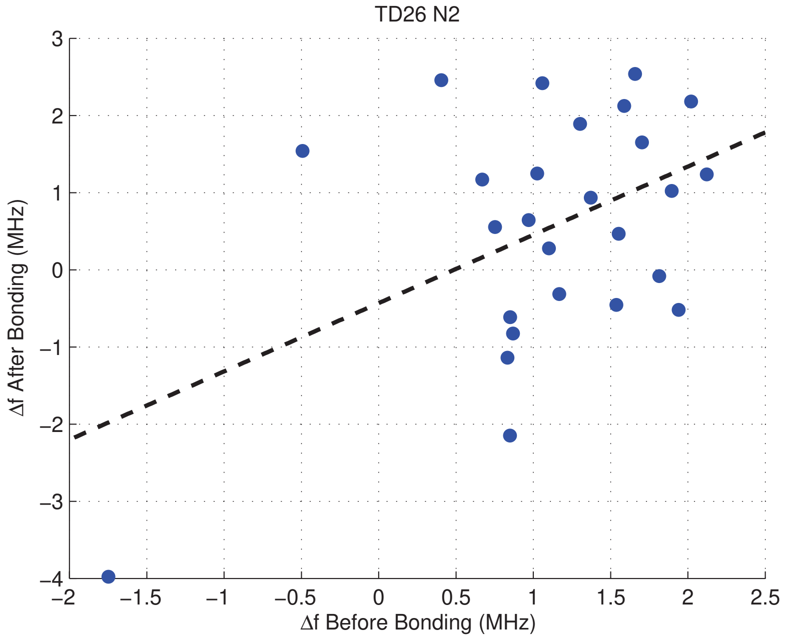

Figure 4.12. Linear correlation between the frequency deviations for TD26 N2 before and after bonding process, $r = +0.47$

CHAPTER 5

CONCLUSION

In this chapter, the conclusions are represented with the verification of methodology by applying the same measurement procedures to TD24 Relax Tolerance structure [35].

5.1. Conclusion

According to microscope measurements, geometrical errors are very small and inside the accuracy of the measuring machine that we are using. Frequency errors are also very small and at the limit of our bead-pull measurement resolution. There is no visible strong correlation between geometrical defects and frequency errors before bonding, but TD26 N2 and N4 show a negative moderate correlation.

On the other side, the frequency deviations before and after bonding seem to be correlate indicating that the cells are not deformed by the bonding process. In general, frequency of all cells is decreasing indicating a better contact and smaller volume after the bonding step.

In order to verify the methodology for investigating the geometrical correlation before bonding, the same measurements and methodology were applied to the TD24 Relax Tolerance structure that was machined with 20 μm tolerance. The 'b' parameter and frequency deviations were measured by the same methods, microscope and bead-pull method as shown in Figure 5.1. The results were obtained as illustrated in Table 5.1. The data shows also a negative moderate correlation.

In general, the quality of the machining is very good and deviations are small and in the order of the metrology measurements accuracy. When translated to resonant frequency deviations they also seem to cause minimum deviations at the level of the measurement resolution.

For next accelerating structure prototypes the inner dimension measurements will be asked from the machining companies and also Coordinate Measurement Machine (CMM) will be used for checking the dimensions with 0.3 μm accuracy.

Table 5.1.: TD24 RT ’b’ parameter measurement and Δf values

Cell No.	**Nominal ’b’ (mm)**	**Measured ’b’ (mm)**	Δb (μm)	Δf **(MHz)**
1	8.615	8.611	4	-5.5224
2	8.602	8.6	2	-0.2863
3	8.589	8.586	3	-0.9569
4	8.577	8.574	3	-1.011
5	8.565	8.56	5	-4.7408
6	8.552	8.55	2	-0.4165
7	8.541	8.537	4	-1.4662
8	8.529	8.527	2	-0.4833
9	8.518	8.513	5	-2.295
10	8.507	8.503	4	-2.0503
11	8.496	8.492	4	-0.7994
12	8.485	8.483	2	1.3326
13	8.475	8.47	5	-3.5785
14	8.465	8.461	4	-0.7611
15	8.455	8.451	4	-1.8191
16	8.445	8.438	7	-2.6465
17	8.436	8.427	9	-1.6992
18	8.426	8.418	8	-2.9696
19	8.417	8.408	9	-3.2823
20	8.408	8.399	9	-0.7752
21	8.399	8.392	7	-1.1454
22	8.391	8.383	8	-2.2996
23	8.383	8.378	5	-0.6128
24	8.375	8.37	5	-1.7271

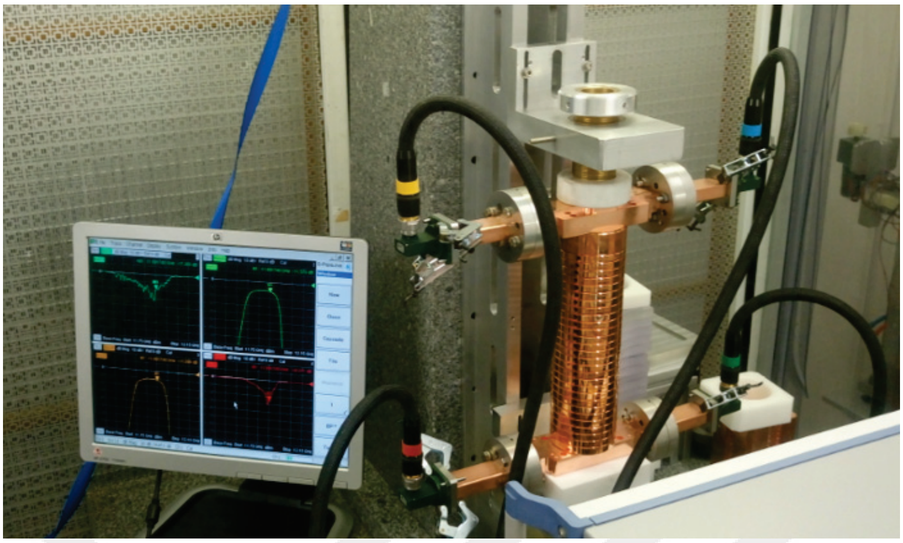

Figure 5.1. TD24 Relax Tolerance Structure under bead-pull measurement

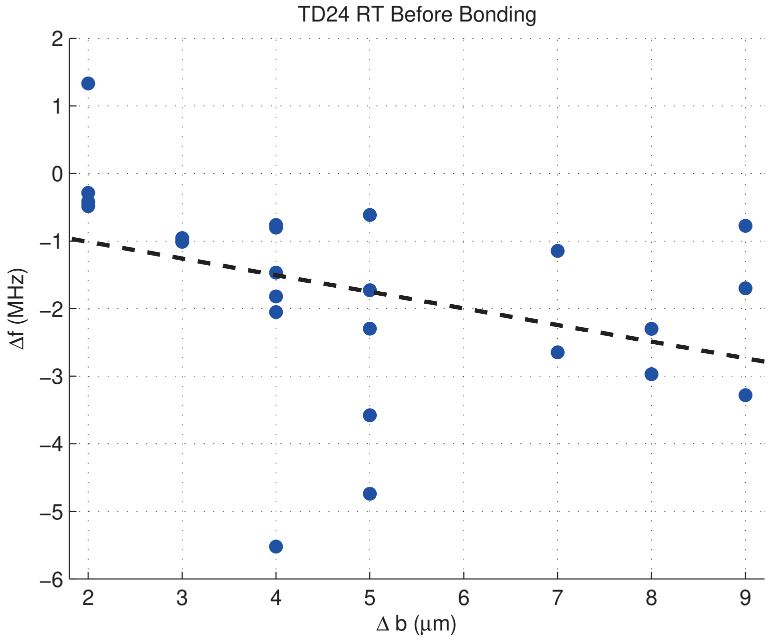

Figure 5.2. Scatterplot for TD24 Relax Tolerance Before Bonding, r = -0.378

REFERENCES

[1] CERN Accelerating Science. https://council.web.cern.ch/en/content/member-and-associate-states-observers (accessed May 27, 2018).

[2] CERN Accelerating Science. https://home.cern/topics/large-hadron-collider (accessed May 28, 2018).

[3] CERN Accelerating Science. http://tlep.web.cern.ch/ (accessed May 28, 2018).

[4] CLIC Study. http://clic-study.web.cern.ch/ (accessed May 28, 2018)

[5] Aicheler, M.; Burrows, P.; Draper, M.; Garvey, T.; Lebrun, P.; Peach, K.; Phinney, N.; Schmickler, H.; Schulte, D.; Toge, N. *A multi-TeV linear collider based on CLIC technology: CLIC Conceptual Design Report* 2014.

[6] Wangler, T. P. *RF Linear Accelerators*; Wiley-VCH Verlag: Weinheim, 2017.

[7] CST - Computer Simulation Technology. https://www.cst.com/ (accessed May 28, 2018).

[8] Liepe, M. *Lecture 19, RF Systems and Particle Acceleration*. P4456/7656, Cornell University, Spring 2010. https://www.classe.cornell.edu/ liepe/webpage/docs/P4456L19.pdf (accessed May 28, 2018).

[9] Weiss, M. *Introduction to RF Linear Accelerators*. CERN Accelerator School: 5th General Accelerator Physics Course, 1992.

[10] Pozar, D. M. *Microwave Engineering*; John Wiley & Sons: Hoboken, 2012.

[11] ANSYS HFSS: High Frequency Electromagnetic Field Simulation Software. https://www.ansys.com/products/electronics/ansys-hfss (accessed May 28, 2018).

[12] 3D Modeling Solutions CATIA^{TM} - Dassault Systèmes®

https://www.3ds.com/products-services/catia/ (accessed May 28, 2018).

[13] Castro, E. R. *Post Mortem Analysis*

[14] Engineering Simulation & 3D Design Software https://www.ansys.com/ (accessed May 28, 2018).

[15] Malabaila, M. *Cleaning Procedure for Copper Parts*, Technical Report, CERN EDMS 1084640.

[16] Hanna, S. *RF Linear Accelerators for Medical and Industrial Applications*; Artech House: Boston, 2012.

[17] Solodko, A. *Baseline Fabrication Procedure: Review and Recent Development*; International Workshop on Breakdown Science and High Gradient Technology (HG2015), Tsinghua University ,16-19 June 2015

[18] Atiyeh, S. *Machining Precision Classification*

[19] Paszkiewicz, J., Private communication.

[20] Grudiev, A., *RF design and parameters of 12 GHz TD24-vg1.8-disk*; Technical Report, CERN EDMS 1068314.

[21] Grudiev, A., *RF design and parameters of 12 GHz TD26_vg1.8_R1_CC*; Technical Report, CERN EDMS 1524527.

[22] Wang, S. H. *RF Electron Linac*. The Fourth OCPA Accelerator School, 2006.

[23] Sadiku, M. N. O. *Numerical Techniques in Electromagnetics*; CRC Press: Boca Raton, 2001.

[24] Jin, J. M. *The Finite Element Method in Electromagnetics*; John Wiley & Sons Inc.: Hoboken. New Jersey, 2014.

[25] Giordanino, L., *12SWV18026-01CSR1CC-STANDARD DISC_TD26_R1_CC*; Technical Report, CERN EDMS 1603911.

[26] Lebet, S.; Gacon, D. *Movable Bead-pull Test Bench*; CERN, 2018

[27] optical microscope / measuring / digital camera / 3-axis non-contact measuring Hawk Duo Vision Engineering Ltd. http://www.directindustry.com/prod/vision-engineering-ltd/product-5580-1085867.html (accessed May 29, 2018).

[28] Steele, C., *IEEE Transactions on Microwave Theory and Techniques* 1968, 16 (11), 973.

[29] Moura, L.; Kitney, R. *Computer Physics Communications* 1991, 64 (1), 57.

[30] Bedolla, J. S. *Inner Radius Measurement Algorithm*

[31] MATLAB - MathWorks. https://www.mathworks.com/products/matlab.html (accessed May 28, 2018).

[32] Shi, J.; Grudiev, A.; Wuensch, W. *Nuclear Instruments and Methods in Physics Research Section A: Accelerators, Spectrometers, Detectors and Associated Equipment* 2013, 704, 14.

[33] Johnson, R. A.; Bhattacharyya, G. K.*Statistics: Principles and Methods*; John Wiley & Sons, Inc.: Hoboken, NJ, 2014.

[34] Statistical Correlation. https://explorable.com/statistical-correlation (accessed May 28, 2018).

[35] Solodko, A., *12SWV18024-__02CS05-STANDARD CELL-TD24 R05 V2*; Technical Report, CERN EDMS 1148071.